ASSESSMENT OF GOVERNING HEAT AND MASS TRANSFER COEFFICIENTS FOR CRYOGENIC NO-VENT TOP-OFF MODELING

ROBERT AHLMAN

Bachelor of Science in Mechanical Engineering

Case Western Reserve University

May 2014

submitted in partial fulfillment of the requirements for the degree

MASTERS OF SCIENCE IN MECHANICAL ENGINEERING

at the

CLEVELAND STATE UNIVERSITY

May 2021

We hereby approve this thesis for

ROBERT AHLMAN

Candidate for the Master of Science in Mechanical Engineering degree for the

Department of Mechanical Engineering

and the CLEVELAND STATE UNIVERSITY'S

College of Graduate Studies by

Thesis Committee Chairperson, Dr. Wei Zhang

Department & Date

Thesis Committee Member, Dr. Yongxin Tao

Department & Date

Thesis Committee Member, Dr. Jason Hartwig

Department & Date

Student's Date of Defense: May 5, 2021

ACKNOWLEDGMENTS

This thesis would not be possible without the support of a whole host of individuals and organizations. I would first like to acknowledge the support of the Ohio Space Grant Consortium Master's Fellowship as well as the Lewis' Educational and Research Collaborative Internship Project at NASA GRC. The financial support provided through these institutions made this work possible. I would like to thank my advisor, Dr. Wei Zhang for her guidance throughout graduate school and her support as I pursued different endeavors to broaden my academic experience. Additionally, I would like to thank Dr. Jason Hartwig whose support, both professionally and personally, made this work possible. I cannot express my appreciation enough to the both of you for your help as I navigated graduate school and NASA these past two years. I would also like to thank my fellow interns at NASA Glenn Research Center for their friendship and help on this work. Specifically, Justin Clark, Zachary Hacker, Shreykumar Jain, and Martin Schmeidler, your assistance with the development and refinement of the UNVF model along with your keen review and sharp questioning have improved the quality of this work immeasurably and I am forever grateful for your input. I would like to thank my family and friends, whose support and encouragement has helped me to continue reaching towards my goals, even when I doubted myself. Finally, I would like to thank my wife, Megan, for her unwavering support as we navigated balancing graduate school with full time work during a global pandemic. I can never thank you enough.

ASSESSMENT OF GOVERNING HEAT AND MASS TRANSFER COEFFICIENTS FOR CRYOGENIC NO-VENT TOP-OFF MODELING

ROBERT AHLMAN

ABSTRACT

No-vent fill / no-vent top-off (NVF/NVTO) is a method to enable the transfer of cryogenic propellants without the need to vent. Transferring propellants in microgravity environments is necessary to support the long-duration space missions planned for the coming decades. A key developmental milestone to developing this capability fully is the simulation and experimentation of NVF/NVTO in 1-g settings. This work seeks to advance the former by assessing the effectiveness of different heat transfer correlations used in a 1-g non-equilibrium model. Heat transfer correlations for natural convection and two-phase boiling heat transfer are compared against experimental results for 34 different tests. Two distinct experiments, comprised of 21 tests, are presented in detail here. These tests cover a variety of different injection methods, receiver tank geometries, receiver tank materials, cryogenic propellants, and initial tank states. Overall for the cases tested in this work, the model was able to predict the pressure response within the receiver tank to a mean absolute percentage error of 25.9%. The temperature response error rate was 29.5% and 24.9% for wall-gas and two-phase nodes, respectively. Compared to the worst case correlation set tested, the pressure prediction error rate represents a 31% improvement. For the cases presented in this work, the mean pressure prediction error rate was 15.5%. Future work could evaluate the effectiveness of this model against experiments conducted with different propellants or different initial conditions. In its current form, however, the model can still be used to help reduce design and testing time for 1-g experiments, enabling the quicker iteration that is necessary to meet the technological demands of future space missions.

TABLE OF CONTENTS

LIST OF TABLES

LIST OF FIGURES

Table I: NOMENCLATURE

Abbreviation	**Definition**
A	Area
C	Specific Heat Capacity
C_d	Discharge Coefficient
D	Diameter
Fr	Froude Number
g	Gravity
Gr	Grashof Number
h	Enthalpy or Heat Transfer Coefficient (denoted in text)
k	Thermal Conductivity
L	Characteristic Length
m	Mass
M	Molar Mass
$\dot{m}$	Mass Flow Rate
Nu	Nusselt Number
P	Pressure
Pr	Prandtl Number
q"	Heat Flux
$\dot{Q}$	Heat Transfer Rate
R	Radius
Ra	Raleigh Number
Re	Reynold's Number
t	Time
T	Temperature
u	Internal Energy
V	Velocity
$\dot{W}$	Work Rate
Greek	**Definition**
α	% Liquid Evaporated from Injector to Wall/Interface
	or Accommodation Coefficient (denoted in text)
β	Fraction of Liquid Incident on Wall that Boils
β_{te}	Coefficient of Thermal Expansion
ϵ	Flashing Coefficient
μ	Dynamic Viscosity
ν	Kinematic Viscosity
ρ	Density
χ	Fraction of Liquid Travelling to Interface vs Wall
Subscript	**Definition**
$cond$	Condensation
d	Droplet
$evap$	Evaporation
g	Gas
i	Interface
in	Tank Inlet
int	Interface
l	Liquid
L	Characteristic Length
R	Radius
tp	Two-Phase
wg	Wall-Gas

CHAPTER I

Introduction

A key technological development necessary to enable longer-term space travel is the ability to refuel in space. Current manned operations are limited in their duration by the trade-off present between payload and propellant masses prior to launch. A concept that has emerged in recent years to address this challenge is that of the cryogenic fuel depot. The depot would serve as a refueling station for spacecraft and could be located at key locations, such as in lunar or low earth orbit. This ability to refuel would give spacecraft the necessary chemical potential energy from cryogenic propellants needed to advance their missions.

In comparison with storable propellants i.e., propellants which are liquid at standard temperature and pressure (STP), cryogens such as liquid oxygen (LOX) and liquid hydrogen (LH2) offer improved performance [1]. Cryogens are substances which occur in a gaseous state at STP but which can be cooled until they change phase to liquid; typically near 100K or less [2]. Common cryogenic propellants include the aforementioned LOX and LH2 as well as liquid methane (LCH4). Though they provide higher energy than storable propellants, cryogens are susceptible to a number of different handling challenges including gradual boil-off and the subsequent tank self-pressurization [3]. In addition to challenges related to the storage of cryogenic propellants, there are also difficulties with how the propellants are transferred from

tank to tank. In many cases, the receiving tank will be at a temperature and pressure which causes flashing and rapid boil-off of the cryogen upon its injection.

To address this, a number of solutions are used. In terrestrial gravity, cryogenic tanks are filled with a vent valve open to prevent pressure build-up. This approach is sufficient in 1g because the location of the liquid and gaseous phases is known. An obvious drawback of this approach in microgravity is that, because of the unknown location of the liquid and vapor phases of the propellant, it is possible the liquid propellant would be vented overboard. This is not only wasteful but could potentially introduce forces from an otherwise non-propulsive vent, causing the spacecraft to unexpectedly change its trajectory [4].

Another option for transferring cryogenic fluids is to pre-chill the receiving tank using a cryocooler. Cryocoolers work following similar thermodynamic principals to standard refrigerators, just at cryogenic temperatures. Once the cryocooler has cooled the receiving tank to a sufficiently cold temperature, propellant transfer can then begin. The inclusion of cryocoolers for spaceflight application has been studied extensively by NASA and has been worked on by both civil servants and private industry alike [5]. Cryocoolers have been shown to be effective in the long-term storage of cryogenic fuels [4] though, due to the lack of natural convection in microgravity, they may not prove effective in cooling down the receiver tank ullage sufficiently to avoid a pressure spike during the transfer process. They also require additional energy input. For these reasons, it is desirable to resolve a way to transfer cryogenic propellant in microgravity that mitigates or removes all of these potential challenges.

One such method is the no-vent fill (NVF) process. In this method, the cryogen is sprayed into the receiver tank in such a way that the spray itself is used to pull energy from the ullage and tank walls. This process may be preceded by a Charge-Hold-Vent (CHV) cycle in which a slug of liquid cryogen is transferred into the tank

(charge), allowed to come to thermal equilibrium (hold), and then released to the atmosphere / space as vapor (vent). CHV can be repeated multiple times until the thermodynamic state of the tank is sufficient to allow for the NVF process to begin. Similar to the NVF process, a no-vent top-off (NVTO) can also be performed. The NVTO is fundamentally the same process as the NVF though the initial conditions are different. While an NVF is initiated with a completely evacuated receiving tank, NVTO is performed when there is some initial amount of cryogenic propellant in the receiving tank. As will be described in upcoming sections, NVTO introduces a new set of challenges due to the thermodynamic non-homogeneity of the liquid and vapor phases within the receiving tank.

These methods are all in service of the development of an in-space propellant depot. While specific architectures will vary across designs, most propellant transfers contain the same four components: liquid acquisition in a storage tank, transfer via insulated lines, receiver tank chilldown, and receiver tank fill. These primary components are illustrated in Figure 1. In the first step, a liquid acquisition device (LAD) is necessary to transfer fluid from the supply tank. This is due to the unknown location of the liquid and vapor phases in microgravity [6]. It is then necessary to chill down the transfer line sufficiently to ensure that single phase liquid enters the receiving tank. Following transfer line chilldown, the receiving tank is then chilled down using the CHV procedure described earlier. The final step in the propellant transfer is to then initiate a no-vent fill.

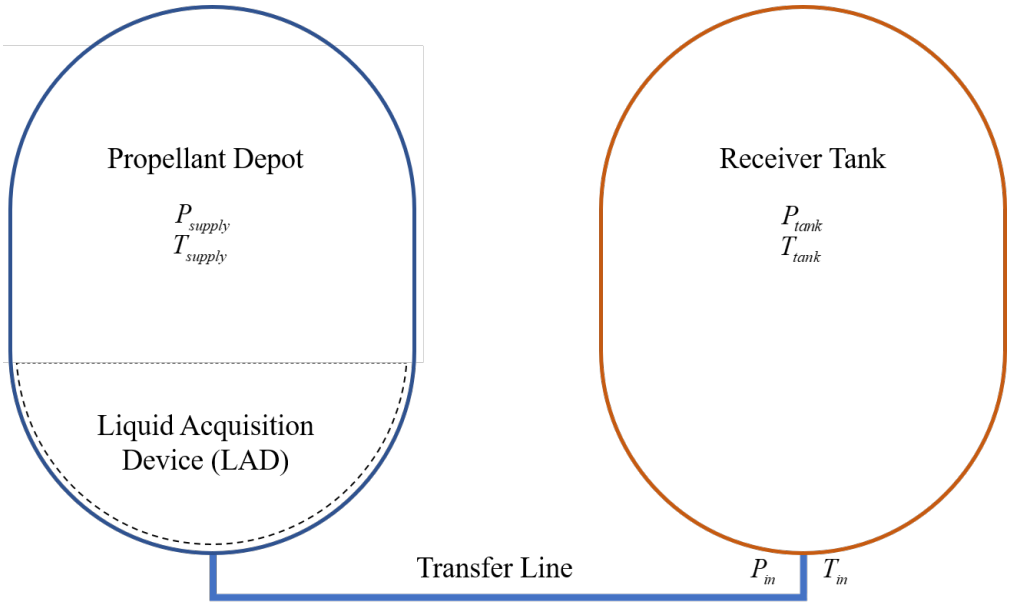

Figure 1: Schematic view of propellant transfer components.

NVF is a well-documented and studied process. A number of different researchers have conducted experiments over the past three decades looking at different combinations of cryogenic fluid, tank shape, and injection method, among other parameters. In an attempt to better understand the thermodynamic and fluid dynamic considerations associated with this process, a Matlab model has been developed to analyze and predict the outcome of a variety of different NVF scenarios in 1g. This model was then run and its output subsequently compared to results of multiple experiments. This work briefly highlights the re-derivation of the model, mostly focused on the inclusion of updated heat transfer correlations for natural convection, droplet boiling at the tank wall, and evaporation and condensation at the liquid/vapor interface. The main focus of this work, however, is to assess the value of these new correlations by modeling more than 20 different experiments, including two sets of experiments that, as of the time of this writing, have not been modeled.

1.1 Model Background

1.1.1 Governing Equations

Details of the Universal No-Vent Fill (UNVF) model used to compare against the NVF/NVTO experiments presented in this work will be more thoroughly described in forthcoming work from Hartwig et al [7]. Only a brief description is presented here to provide necessary context. To achieve a generalized model, it was necessary to account for a multitude of the most commonly used parameters present in most NVF/NVTO experiments. This includes multiple injectors, tank materials, tank geometries, and cryogenic liquids. These parameters are accounted for in the governing equations, which in turn are derived based on the control volumes (CVs). Of the eight control volumes or nodes in the code, five represent open control volumes (droplet, droplet interface, vapor, liquid, and liquid/vapor interface) and three are closed CVs (hot wall, two-phase wall, and cold wall). At each time step within the code, values for the heat and mass transfer across control volume boundaries are calculated.

The model tracks the evolution of the injected mass through flashing, evaporation, and boiling. Once the liquid cryogen is injected, some portion (ϵ) immediately flashes. The value of ϵ is determined thermodynamically based upon the incoming liquid temperature and pressure as well as the RT temperature and pressure. From there, any remaining liquid is able to evaporate in transit to the wall or liquid vapor interface, denoted as α. Finally, based on the specific trajectory of the chosen injector, the remaining liquid is then directed to either the wall where it is available to boil ($\chi \cdot \beta$) or it enters the liquid node via the interface ($1-\chi$). This is seen pictorially in Figure 2.

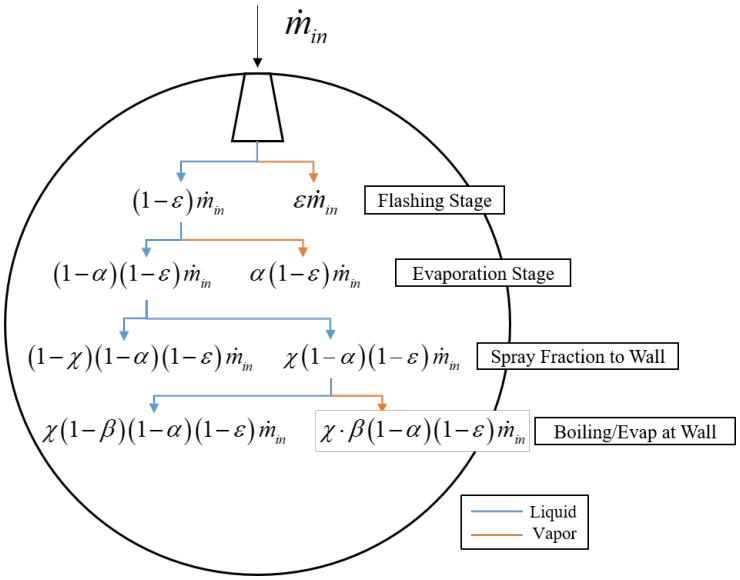

Figure 2: Changes of state of matter present in model.

The reduced set of governing equations for mass and energy used in the model are as follows:

$$\frac{dm_g}{dt} = \left[\epsilon + \alpha(1-\epsilon) + \chi\cdot\beta(1-\alpha)(1-\epsilon)\right]\dot{m}_{in} + \dot{m}_{int,evap} \tag{1.1}$$

$$\frac{dm_l}{dt} = \left[\chi(1-\beta)(1-\alpha)(1-\epsilon) + (1-\chi)(1-\alpha)(1-\epsilon)\right]\dot{m}_{in} - \dot{m}_{int,evap} \tag{1.2}$$

$$\frac{d\left(m_l u_l\right)}{dt} = \dot{Q}_{il} - \dot{W}_{lg} + (1-\beta\chi)(1-\alpha)(1-\epsilon)\dot{m}_{in}h' - \dot{m}_{int,evap}h_f \tag{1.3}$$

$$\begin{aligned}\frac{d\left(m_g u_g\right)}{dt} &= \dot{Q}_{wg} + \dot{Q}_{tp} - \dot{Q}_{gi} - \dot{Q}_{gdi} + \dot{W}_{lg} + \epsilon\dot{m}_{in}h_{in} \\ &+\alpha(1-\epsilon)\dot{m}_{in}h_g + \chi\cdot\beta(1-\alpha)(1-\epsilon)\dot{m}_{in}h_g + \dot{m}_{int,evap}h_g\end{aligned} \tag{1.4}$$

$$m_{tp}C_{tp}\frac{dT_{tp}}{dt} = -\dot{Q}_{tp} \pm \dot{Q}_{cond} \tag{1.5}$$

$$m_{wg}C_{wg}\frac{dT_{wg}}{dt} = -\dot{Q}_{wg} - \dot{Q}_{cond} \tag{1.6}$$

1.1.2 Method of Solution

Equations 1.1 - 1.6 are discretized and solved at each time step. This is done using an iterative relaxation technique e.g., Gauss-Seidel, where values from the previous iteration are used to initiate the current calculations. In the equations above, there are 6 unknowns which are resolved using this technique. These variables are the vapor and liquid masses, $m_g(t)$ and $m_l(t)$, liquid density $\rho_l(t)$, tank pressure $P(t)$, and the gas and two-phase wall node temperatures, $T_{wg}(t)$ and $T_{tp}(t)$. As parameter values are updated, they are immediately used in the subsequent calculations. Because some of these variables of interest are implicit in multiple equations e.g., $\rho_l(t)$, it is necessary to solve these equations simultaneously within the numerical method used for the other variables of interest. To do this, a straight-forward bisection technique was used to arrive at the root value before moving on to the next variable of interest.

1.2 Literature Review

The concept of a fuel depot for long-duration space travel is not new. Work has been done since the early years of human spaceflight outlining concepts for orbiting cryogenic fuel depots and their associated hazards [8]. In more recent decades, a significant body of work has been produced discussing the development need for these depots. In 2006, Howell et al [9] discussed the necessary research and development (R&D) objectives as well as system planning considerations needed for an on-orbit depot. This work proposes the specifications for a fuel depot which would be stationed in LEO. The R&D paths noted in the work, notably zero boil-off of cryogenic propellant and low-gravity mass-gauging, are all current research projects with promising paths. While propellant transfer is noted as a necessary technological advancement, it is not discussed in much depth.

Another fuel depot concept was proposed by Schweickart in 2014 [10]. In this

proposal, analysis was also conducted related to the actual thermodynamics of the propellant transfer. The analysis was conducted using SINDA-FLUINT [11] and the results were validated against experiments conducted by Dr. David Chato at NASA Glenn Research Center in 1991 [12]. While these experiments were conducted in 1-g, Schweickart extrapolated the SINDA-FLUINT model to 0-g operations based hypothesized operational parameters used for the fuel depot as well as assumptions related to the liquid location as a function of fill level in the supply tank, which has been fitted with a propellant management device in the proposed concept. As a first order approximation, this approach lends credence to the promise of the fuel depot concept. Some drawbacks are clearly present in this work, however, which the model used in this work seeks to address. Firstly, SINDA-FLUINT does not allow the tracking of droplets through the RT ullage. Because of this, the effect of different injectors and injection methods cannot be evaluated. Important parameters, such as the heat and mass transfer of the droplets with the warm ullage are missed.

Experiments conducted since 1991 have used a variety of different injection methods, tank shapes, tank materials, and fill conditions. An appropriately validated model of propellant transfer, therefore, must be able to accommodate the different situations presented in these works. As noted in the work by Schweickart, Chato conducted transfer tests at NASA GRC in 1991 [12], expanding upon work conducted in 1990 [13]. These experiments were conducted with both LN2 and LH2 and used both top and bottom injection methods. While some cases reported in these experiments had full time-series data associated with the fill response, the inlet parameters during all experiments were largely reported as average parameters. A clear drawback of trying to model cases with fixed inlet parameters is that it can override natural tank responses. As an example, fixing the mass flow rate when modeling a case with a fixed supply tank pressure will tend to over-predict the mass flow rate when the

RT pressure spikes at the beginning of fill and then under-predict the mass flow rate later in the fill when the RT pressure has subsequently reduced. This is evident when looking at the discharge coefficient equation 1.7.

$$\dot{m_{in}} = C_d \rho_l A_{in} \sqrt{\frac{2\left(P_{supply} - P_{tank}\right)}{\rho_l}} \tag{1.7}$$

For this reason, constant $\dot{m}$ cases were not used for model validation. While the experiments in Chato 1991 provided time-series inflow data, Chato 1990 only supplied average inflow values. Therefore these experiments were not used for model validation or correlation assessment. In addition to the experiments conducted by Chato et al in 1990 [13], experiments conducted by Chato in 1993 [14], and Moran and Nyland in 1991 [15] and 1992 [16] all suffer from the same drawback of only supplying average inflow data. These experiments all provide interesting datasets which fully-developed models might use for further study, but the lack of inlet condition data precludes them from study here.

Fortunately, a host of NVF/NVTO experiments exist which have the information necessary to use them for model validation and correlation assessment. In this work, data from two different sets of experiments are presented and used to assess the performance of different heat transfer correlations in the UNVF model. These two datasets, as well as the various different heat transfer correlations used when modeling them, will be described in detail in the following sections.

1.3 Thesis Overview

This work is meant to achieve two primary goals. Firstly, it is meant to share a high-level overview of the Universal No-Vent Fill model development, specifically as it relates to the subroutine correlation assessment that was performed by the author. Secondly, and more importantly, it is meant to share the results obtained when the

UNVF code was used to model two historical datasets. The organization of this thesis is such that each chapter following the correlation assessment deals with a single historical dataset.

For the subroutine development section, time is first spent developing and explaining the relevant underlying fluid physics. This is done to provide context for a reader who may not have a background in the specific subject matter at hand. This overview is not meant to be exhaustive and as such it is recommended that the reader review the cited papers and textbooks for a more thorough understanding. Not all of the model subroutines are explored in this section. Rather, it is meant only as an overview of some of the subroutines worked on most by the author. The reader is referred to the aforementioned forthcoming works by Hartwig et al for a more detailed account of the model.

Having described at a high level the underlying physical phenomena for a given section, a brief literature review is then provided. This literature review shares the sources of the correlations tested in this model. Where necessary, additional information is given to explain how various different correlations were combined to produce a correlation that would be suitable for the purposes of this model.

The correlation assessment methodology is described next. This section is meant to show how the correlation sets were organized as well as the specific correlation combinations that were tested. Due to the complex interactions between the different subroutines in the model, it was decided that it was necessary to test 100% of the correlation combinations. An exception was granted, however, to the analysis of the equilibrium / non-equilibrium assumption regarding evaporation and condensation at the liquid-vapor interface as well as the evaluation of an additional correlation for the heat transfer from the ullage to a droplet in flight. This second assessment was done for purely pragmatic reasons since the computing time that would

have been necessary to evaluate all options in one pass was not feasible.

Finally, the results of the correlation assessment are provided. These results are given both in the aggregate and with an eye towards how performance changed based on different test parameters e.g., cryogen used. To arrive at the most generalized version of the model possible, weighting was applied to the various response variables in a manner which the author and collaborators deemed reasonable. This weighting scheme and its implications are discussed in this section.

Following the explanation of the subroutine correlation assessment, the model output is compared to the experimental results for two different datasets, each containing multiple tests. This comparison is broken into two chapters, one for each dataset. While each chapter will become the focus of its own, more in-depth paper in the future, the model development and background sections are omitted from the chapters for the sake of readability and brevity and because they are covered earlier in this work. Instead, each chapter contains the following sections: Experimental Description, Model Inputs/Considerations, and Results.

The Experimental Description and Model Inputs/Considerations sections provide context related to each experiment. Factors such as the tank geometry, fill parameters, and overall experimental objectives are described here. In many cases, more thorough papers exist which detail the specifics related to each experiment. The relevant citations are provided where available in these cases.

In the Results section of each experimental chapter, the model output is compared with the original data from the experiment. Model performance is then assessed and presented using straight-forward error calculations.

CHAPTER II

Correlation Assessment

2.1 Selected Subroutine Development

2.1.1 Natural Convection

Fluid Physics Overview

Natural convection is the phenomenon of heat transfer caused by variations in density which are in turn caused by temperature gradients within a fluid medium. In a traditional case with a fluid sitting atop a heat source, as temperature increases in a given fluid and it subsequently expands, density is decreased. This fluid packet then rises due to the difference in density. Once at the top, the fluid cools once more and begins sinking towards the heat source to being the cycle again. In the case of tanks holding the cryogens, this process is reversed and, given enough time to settle, would result in a thermally stratified tank.

In the NVF and NVTO models, natural convection plays in important role in the heat transfer between the tank wall and the gas node. The model calculates several important dimensionless parameters related to natural convection. The first which merits description is the Prandtl number, which is a ratio of viscous diffusivity, ν, to thermal diffusivity α.

$$Pr = \frac{\nu}{\alpha} \tag{2.1}$$

In addition to the Prandtl number, the Grashof number was also calculated. The Grashof number represents the ratio of buoyancy forces relative to viscous forces acting on a fluid.

$$Gr = \frac{g\beta_{te}\Delta T D^3}{\nu^2} \tag{2.2}$$

where g is gravitational acceleration, β_{te} is the coefficient of thermal expansion, ΔT is the difference in temperature between the wall and the ullage, D is the tank diameter, and ν is the kinematic viscosity of the gas. These two equations (2.1 and 2.2) are then multiplied to calculate the Rayleigh number (Ra) which itself serves as a descriptor of the fluid flow under natural convection forces. The calculation of the Prandtl, Grashof, and Rayleigh numbers is in service of determining a Nusselt number. The Nusselt number is the ratio of convective to conductive heat transfer and is calculated as shown below.

$$Nu = \frac{hR}{k} \tag{2.3}$$

In Equation 2.3, R is the tank radius, k is the fluid's thermal conductivity, and h is the convective heat transfer coefficient. h is the value that is subsequently used to calculate the heat transfer between the wall and the ullage. In order to calculate the Nusselt number, most convective heat transfer correlations rely on expressions of the form $\overline{Nu} = C(Ra)^n$ where C and n are empirically-determined constants.

As will be described in the following section, the previous version of the NVF code relied on natural convection correlations obtained from elliptical horizontal tubes and fitting parameters applied to a subset of experimental data. Evident in Equations 2.2 and 2.3, natural convection heat transfer is highly dependent on geometry.

Therefore it was desirable to evaluate/update the correlations being used in the determination of the convective heat transfer coefficient to ones more analogous to the tank geometries used experimentally.

Natural Convection Literature Review

A number of different correlations were assessed for their applicability to the natural convection within the tanks. While a significant number of sources exist for natural convection correlations in non-cryogenic mediums, the set of correlations available which were determined using cryogenic data is substantially more limited. Yang and West [17] used CFD to determine the heat transfer coefficient within cryogenic propellant tanks. These tanks were modeled as straight cylinders with domed ends, similar to the design of many tanks used in experiments. Based on their work, they determined that existing horizontal and vertical plate correlations in both laminar and turbulent regimes (as determined by the Rayleigh number) over-predicted the Nusselt number. The correlations they developed from their study required the introduction of a characteristic length, such that the Rayleigh and Nusselt numbers were calculated as shown in Equation 2.4, where R is the tank radius and L is the height of the ullage within the tank.

$$Nu_L = \frac{L}{R} Nu_R \quad \text{and} \quad Ra_L = \left(\frac{L}{R}\right)^3 Ra_R \tag{2.4}$$

Ultimately, Yang and West determined natural convection correlations for both wall-liquid and wall-ullage nodes within the tank. The primary limitation of the correlations developed Yang and West is the lack of information regarding the fluid that was modeled. It appears, based on the fluid properties noted in the paper, that the modeled fluid was LH2 though this was not confirmed for this work. The final correlations, along with those from other sources, are listed in Table II for conciseness.

Long and Zhang [18] developed a correlation for supercritical Helium and validated it against experimental and model results. They found that Nusselt number varied exponentially with Rayleigh numbers which was consistent with other literature above a threshold Ra value. A correlation was developed by Daney [19] for LH2 using cylindrical tanks with flat ends though it only covered a somewhat limited range of Rayleigh numbers, $5 \times 10^9 < Ra < 7 \times 10^{12}$. This work also included correlations that were generalized for liquid deuterium convection in spheres, vertical cylinders, horizontal cylinders, and hemispheres.

In addition to cryogen-focused correlations, a number of other heat transfer correlations were gathered in order to fill out the understanding of geometry on natural convection. McAdams[20] developed correlations for vertical and horizontal flat plates under both turbulent and laminar conditions. The vertical flat plates were used to mimic the wall convective heat transfer and the horizontal flat plate convection was used as a proxy for the liquid-vapor interfacial heat transfer. Additional vertical flat plate correlations are available from Eckert and Jackson[21]. Another source of non-cryogenic correlations which were of particular interest were those developed by Guyer related to spherical geometries [22]. These correlations are also used in SINDA/FLUINT [11], the code base which underlies the thermal analysis tool, Thermal Desktop. Chow and Akins [23] also developed spherical geometry relations, looking specifically at laminar wall interactions with water. Mattor et al [24] did similar work with air and helium as the working fluids and under turbulent interactions with the spherical walls.

Table II: Natural convection correlations of the form $\overline{Nu} = C * Ra^n$

C	n	Ra Range	Geometry	Cryogen?	Fluid	Source	Other
0.642	0.167	$Ra_L \leq$ 1e7	Cylindrical w/hemispherical ends	Yes	Unknown	[17]	Liquid-Wall
0.167	0.25	1e7 $< Ra_L \leq$ 1e10	Cylindrical w/hemispherical ends	Yes	Unknown	[17]	Liquid-Wall
0.00053	0.5	1e10 $< Ra_L \leq$ 5e13	Cylindrical w/hemispherical ends	Yes	Unknown	[17]	Liquid-Wall
4.5	0	$Ra_L \leq$ 1e7	Cylindrical w/hemispherical ends	Yes	Unknown	[17]	Gas-Wall
0.08	0.25	1e7 $< Ra_L \leq$ 1e12	Cylindrical w/hemispherical ends	Yes	Unknown	[17]	Gas-Wall
0.0053	0.333	Unknown	Cylindrical w/flat ends	Yes	LHe	[18]	
0.0055	0.379	5e9 $< Ra <$ 7e12	Cylindrical w/flat ends	Yes	LH2	[19]	
0.162	0.327	2e9 $< Ra <$ 5e10	Sphere	Yes	LN2	[19]	
0.104	0.352	7e8 $< Ra <$ 6e11	All Shapes	Yes	LH2,LD2,LN2	[19]	Multiple Fuels
0.59	0.250	1e4 $< Ra <$ 1e9	Vert. flat plate	No	Air	[20]	Laminar
0.13	0.333	1e9 $< Ra <$ 1e13	Vert. flat plate	No	Air	[20]	Turbulent
0.54	0.250	1e5 $< Ra <$ 2e7	Horz. flat plate	No	Air	[20]	Laminar, Above hot surface
0.14	0.333	2e7 $< Ra <$ 3e10	Horz. flat plate	No	Air	[20]	Turbulent, Above hot surface
0.27	0.250	3e5 $< Ra <$ 3e10	Horz. flat plate	No	Air	[20]	Laminar, Below hot surface
0.555	0.250	$Ra <$ 1e10	Vert. flat plate	No	Air	[21]	Laminar
0.021	0.400	1e10 $< Ra <$ 1e12	Vert. flat plate	No	Air	[21]	Turbulent
0.59	0.250	1e4 $< Ra <$ 1e9	Sphere	No	Unknown	[22]	
0.13	0.333	1e9 $< Ra <$ 1e13	Sphere	No	Unknown	[22]	
0.8	0.300	7.74e4 $< Ra <$ 1.13e7	Sphere	No	H2O	[23]	Laminar
1.3127	0.206	1e6 $< Ra <$ 1e8	Sphere	No	Air/He	[24]	Turbulent

These correlations are plotted, grouped by relevant geometry and fluid state in Figures 3, 4, and 5.

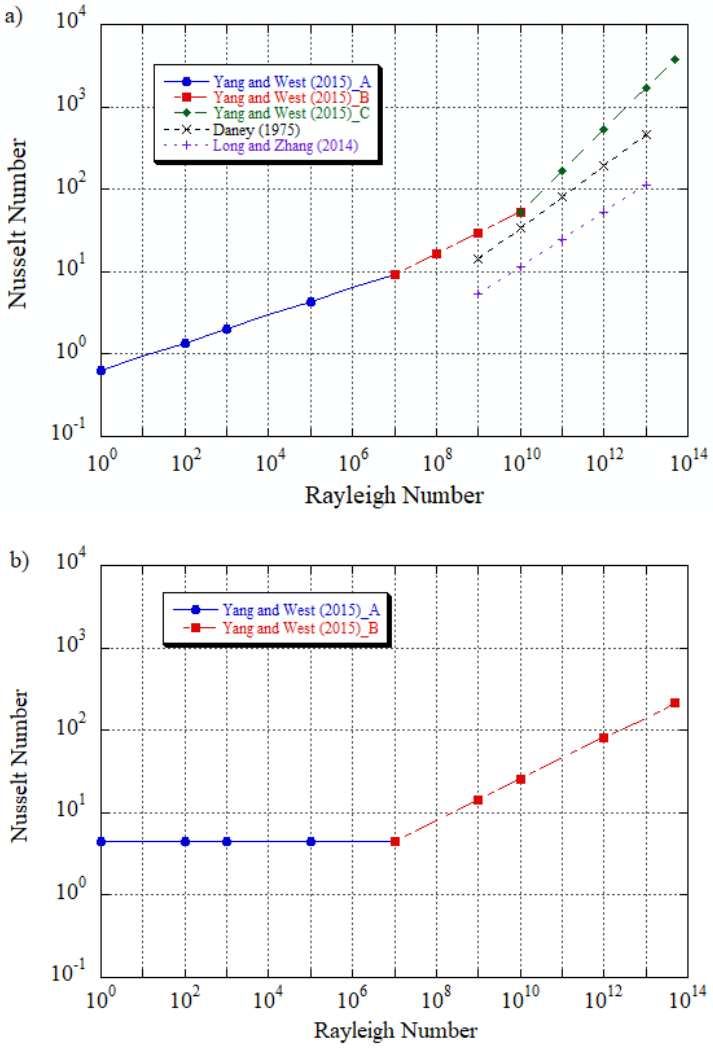

Figure 3: Natural convection correlations for cylindrical tanks relating (a) liquid-wall interactions and (b) vapor-wall interactions

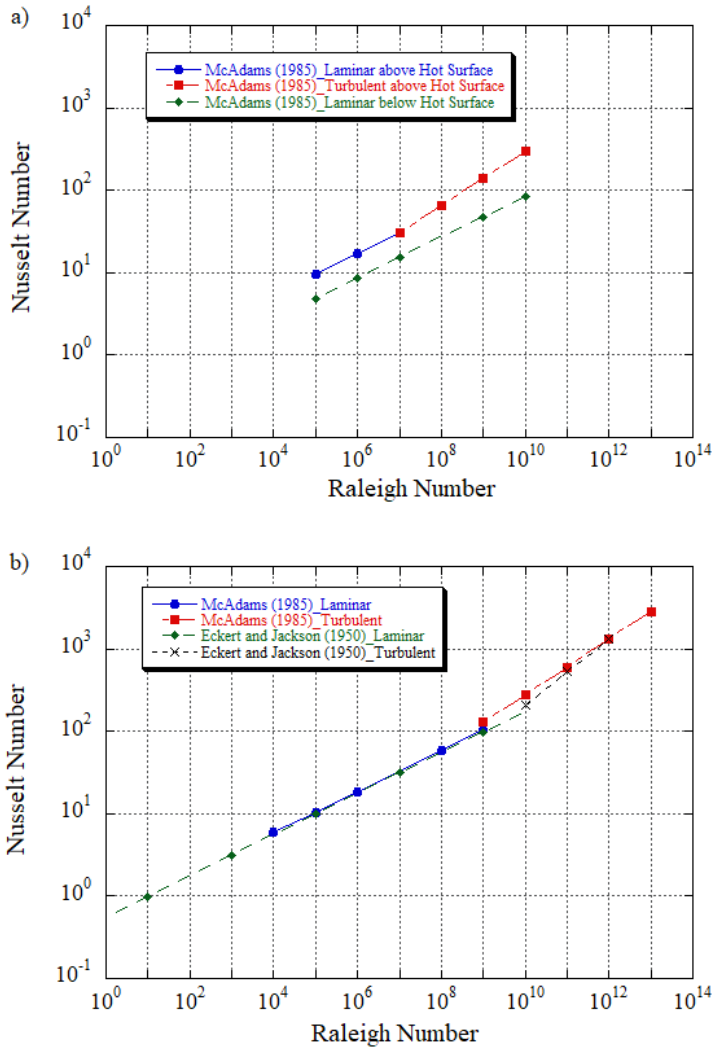

Figure 4: Natural convection correlations for (a) horizontal and (b) vertical flat plates

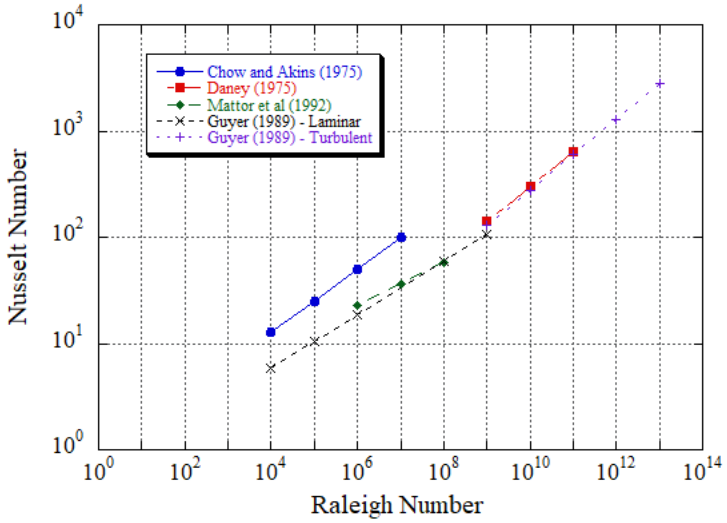

Figure 5: Natural convection correlations for spherical tanks

In addition to these newly incorporated natural convection subroutines, the preexisting correlations were also tested against the experimental data. The format of the preexisting correlations differ from the previously described form of $\overline{Nu} = C * Ra^n$ and are segmented based on application in the model. The segmentation used in the model as described in Section 1.1 are interface to liquid heat transfer, vapor to interface heat transfer, and wall to vapor heat transfer.

To model heat transfer across an agitated liquid/vapor interface, the original model used the following correlation from Memory et al [25].

$$Nu_{il} = C_0 \left(\frac{\rho_l(\rho_l - \rho_g) g h_{fg} L_c^3}{\mu_l k_l \Delta T} \right)^{C_1} \tag{2.5}$$

This equation can be rewritten in terms of Gr (2.2), Pr (2.1), and a dimensionless number A that expresses the changes in energy density from the interface to the liquid. A is defined as follows where ΔT is the temperature difference of the interface (assumed in this correlation to be at saturation) and the liquid, i.e., $T_{sat} - T_l$.

$$A = \left(\frac{(\rho_l - \rho_g) h_{fg}}{\rho_l (\beta \Delta T)(C_{pl} \Delta T)} \right) \tag{2.6}$$

Simplifying 2.5 in terms of dimensionless parameters yields an expression of the following form, where C_0, C_1, and C_2 are defined in Table III.

$$Nu_{il} = C_0 (GrPrA)^{C_1} = C_0 Ra^{C_1} A^{C_2} \tag{2.7}$$

An obvious limitation of this correlation is that it does not account for the effect of fluid momentum on agitation of the interface. This agitation is known to generate larger heat transfer at the interface, thus collapsing pressure more effectively. For submerged injectors, this effect diminishes as liquid level rises and the injected fluid momentum is no longer enough to break / agitate the liquid/vapor interface. To account for this momentum from the injection method, the Froude number, Fr, is included in the correlation. Fr is defined as shown in Equation 2.8.

$$Fr = \frac{V_{in}^2}{g L_c} \tag{2.8}$$

where V_{in} is defined as the injected fluid velocity, g is gravity, and L_c is the distance from the injector exit plane and the liquid/vapor interface. On inspection, one notices that when L_c is small i.e., the distance from the injector exit plane to the liquid/vapor interface is short, Fr is large. As the liquid/vapor interface rises in the tank, Fr will consequently decrease. This phenomenon is also evident in top spray injection methods, though in reverse order. Top spray injection will cause increasing interface agitation as the interface rises in the tank because the distance to the injector exit plane is decreasing. Following the inclusion of Fr, Equation 2.7 is expressed in its final form shown below.

$$Nu_{il} = C_0 Ra^{C_1} A^{C_2} Fr^{C_3} \tag{2.9}$$

In the actual calculation of h_{il} from Equation 2.9, it is important to note that the value of R shown in Equation 2.3 is replaced with a characteristic length, L_c, defined as the interfacial area divided by the cross-sectional area of the tank, $A_{int}/2\pi R$. Equation 2.9 was also used in the baseline version of the model to calculate the vapor-interface heat transfer coefficient. The primary difference was that the terms were calculated with gas properties.

To calculate the heat transfer coefficient between the vapor and tank wall in the baseline model, a similar methodology was applied. In comparison to the interfacial heat transfer correlations, the vapor-wall correlation did not require the inclusion of the Froude number as injected fluid momentum is not a contributing factor. Similarly, A as defined in Equation 2.6 was not necessary. Instead of these parameters, a new ratio, C_r, was proposed in the baseline model. As shown in Equation 2.10, C_r is the ratio of the stored energy in the tank wall to the stored energy in the vapor.

$$C_r = \frac{C_{wall}}{C_g} \tag{2.10}$$

Thus the final form of the correlation used in the baseline model is shown in Equation 2.11, where C_0, C_1, and C_2 are parameters fit to a subset of experimental data. These values are listed in Table III.

$$Nu_{wg} = C_0 Ra^{C_1} C_r^{C_2} \tag{2.11}$$

Table III: Fitting parameters for natural convection correlations used in original model

Coefficient	h_{il}	h_{gi}	h_{wg}
C_0	6.6e5	6.6e5	0.0058
C_1	0.31	0.31	0.4575
C_2	-0.184	-0.184	0.2651
C_3	0.148	0.148	-

2.1.2 Spray Cooling Heat Transfer

Fluid Physics Overview

Spray cooling is a method of cooling which enables high heat fluxes in comparison to other modes of cooling [26]. This is due to the unique interactions taking place between liquid droplets and the surface being sprayed. When a large temperature gradient exists between a surface and a surrounding liquid, a vapor barrier is formed between the liquid and the surface. This has the effect of significantly reducing the heat transfer from the surface [27]. Spray cooling uses the droplet momentum to break through the film layer, thus enabling higher heat transfer rates.

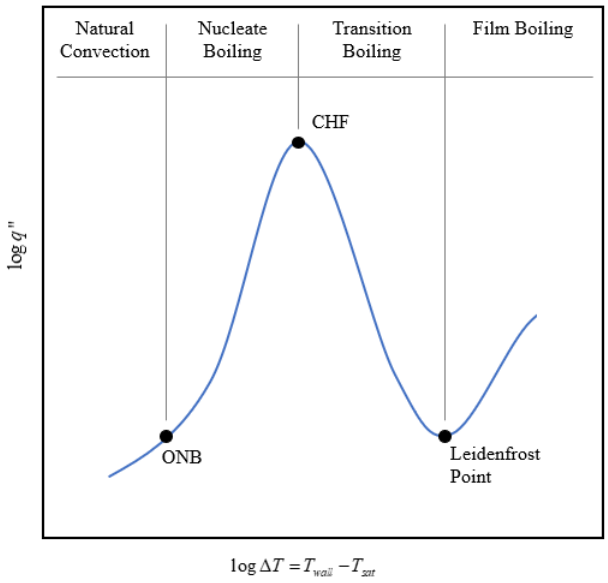

Figure 6: Typical boiling curve showing heat flux vs wall superheat

To understand the heat transfer stages of a surface subjected to spray cooling, a boiling curve is useful. Shown in Figure 6, the boiling curve can be broken into four characteristic sections. In boiling situations, one moves left to right along the x-axis in Figure 6 whereas in quenching scenarios, ones moves right to left. Therefore, in a quenching scenario the first heat transfer regime encountered by cryogenic fluids

is typically film boiling. Film boiling represents the regime with the highest relative wall superheat. In this regime, there is not a liquid-solid interface since the solid surface is covered with a vapor blanket. The primary mode of heat transfer in film boiling is therefore not convection to the liquid but conduction and radiation to the vapor. In this regime, heat transfer is generally much lower than in nucleate boiling. Given the relatively much lower temperatures of cryogenic propellants, they are often in the film boiling regime when first introduced to a superheated surface.

As the difference between wall and liquid temperature decreases, the heat transfer moves to the transition boiling regime. Transition boiling, sometimes referred to as partial film boiling, is an unstable process which is characterized by a mix of nucleate boiling phenomena and film boiling phenomena. In this phase, pockets of insulating vapor are retained at the liquid-solid interface. These insulating areas in turn decrease the overall heat transfer from the surface. The demarcation between transition boiling and film boiling is marked by the Leidenfrost point. This point denotes the minimum heat flux along the curve. As one moves further to the left along the boiling curve from the Leidenfrost point, the heat flux continues to increase. This is largely due to the proportional decrease in coverage of these insulating vapor pockets at the interface.

Eventually, an inflection point is reached. This maximum is known as the Critical Heat Flux CHF. At this point, the heat transfer from the surface to the liquid is maximized as the number of vapor bubbles carrying heat away from the surface is at its peak. As the wall superheat, ΔT, decreases from CHF, so too does the number of vapor bubbles formed at the liquid-solid interface.

As ΔT decreases from CHF, nucleate boiling becomes the predominant mode of heat transfer. In nucleate boiling, vapor bubbles are formed at the solid-liquid interface. In pool boiling situations, i.e., when the bulk liquid sits undisturbed on

the heated surface, these bubbles then rise through the bulk liquid due to natural convection, eventually breaking the upper liquid surface. In spray cooling scenarios, however, significant interaction takes place between the rising bubbles and the impinging droplets. Rini et al [28] found that the interaction between the rising bubbles and impinging droplets led to the creation of secondary bubble nuclei within the bulk liquid. This phenomenon was found to increase the overall heat transfer for both nucleate boiling and convective heat transfer processes.

Finally, as the temperature difference between the liquid and wall decreases sufficiently, natural convection becomes the primary means of heat transfer (see subsection 2.1.1). This transition between natural convection and nucleate boiling is known as the Onset of Nucleate Boiling of ONB.

Spray Cooling Literature Review

While pool boiling has been extensively studied for cryogenic and non-cryogenic fluids alike, a distinct lack of data exists for cryogenic spray cooling. Some cryogenic spray cooling work has been performed by Sehembey [29][30] and Awonorin [31], though the correlations developed in their work were not suitable to use in the development of this model as will be discussed later.

In the case of spray cooling, significantly more work has been conducted using water and other room-temperature fluids as compared to cryogenic fluids. For a much more comprehensive review of literature related to spray cooling, the reader is referred to a two part work conducted by Liang and Mudawar in 2017 [32][33]. This work compiles a number of correlations developed for room-temperature spray cooling across the different heat transfer regimes on the boiling curve. The correlations presented in this work were tested as a part of the overall correlation assessment. A distinguishing feature of the boiling curves developed by Liang and Mudawar is

the distinction between cases which include a film-wetting regime and cases which do not. To verify the continuity of the boiling curves created by these correlation sets, plots were made of each case as shown in Figure 7. One important note as it relates to all of continuity-check plots is that the exact values for heat flux as well as critical locations along the curve such as CHF and the Leidenfrost point, are highly variable based upon the input parameters. The continuity plots presented here are not intended to show a well-generalized representation of the boiling curves for the different fluids under evaluation. One thing that becomes very clear though when looking at Figure 7 is that the location of the Leidenfrost point and Critical Heat Flux is closer to that of water, as compared with LN2 or LH2. This highlights the obvious shortcoming of the lack of cryogenic spray cooling data available.

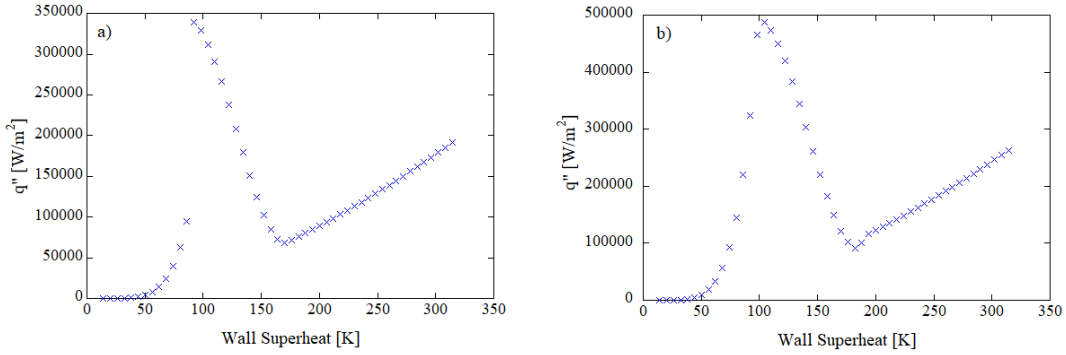

Figure 7: Continuity check on boiling curves produced by correlations presented in [32][33]. Subplot (a) shows the boiling curve without the film-wetting regime while (b) includes the film-wetting regime.

In addition to the correlations presented in Liang and Mudawar's work, two other sets of correlations were tested as part of the overall correlation assessment. The second set of correlations tested is comprised of separate correlations for LH2 and LN2. To model LH2, correlations developed by Lei et al [34] were used. In the original work, these correlations were used to model tank pressure responses in both

normal and microgravity conditions. In this work however, they are only used to help assess pressure responses in 1-g. Because the correlations developed in [34] were only applicable to LH2, it was decided to include correlations to model LN2 in this correlation set. These were obtained from a separate, pre-validated code. This code was developed by researchers at NASA GRC and uses work done by Baumeister and Simon [35], Lienhard and Dhir [36], Shirai et al [37], Minchenko et al [38], and Wang et al [39] to construct a boiling and quenching curve for LN2. Additionally, it was used to a high degree of success in work by Majumdar et al [40]. In a manner similar to what was done with the correlations developed by Liang and Mudawar, the second set of spray cooling correlations were plotted after being programmed into the model to check for continuity. These are shown in Figure 8.

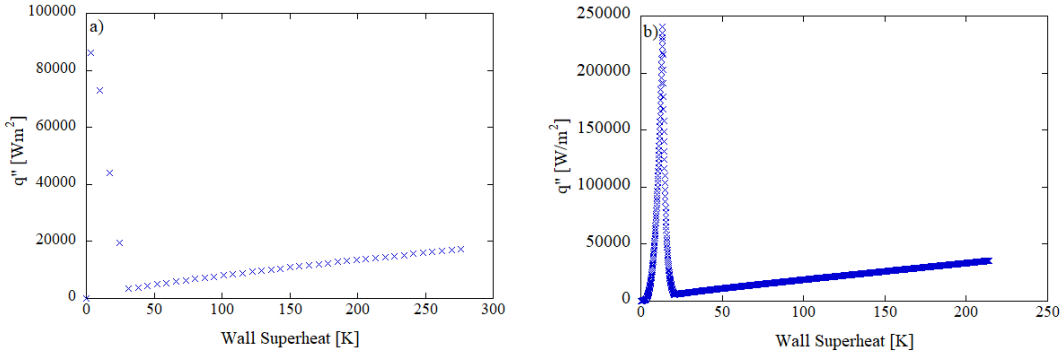

Figure 8: Continuity check for the second set of spray cooling correlations for (a) LH2 and (b) LN2.

The third and final set of spray cooling correlations which were tested are a hybrid of correlations developed in two different papers, one by Mudawar and Valentine in 1989 [41] and the other by Klingzing et al in 1992 [42]. In the case of this correlation set, Mudawar and Valentine correlations are used to define the portion of the curve at lower ΔT, specifically from the onset of nucleate boiling up to CHF. Klingzing et al is then used to define the film boiling the regime from the

Leidenfrost point on up. In order to smoothly connect the two sections of the curve, a simple linear interpolation was used to define the transition boiling regime as shown in Equation 2.12.

$$q"_{TB} = \left(\frac{q"_{MIN} - q"_{CHF}}{\Delta T_{MIN} - \Delta T_{CHF}} \right) (\Delta T_f - \Delta T_{CHF}) + q"_{CHF} \tag{2.12}$$

The resultant boiling curve is shown below in Figure 9

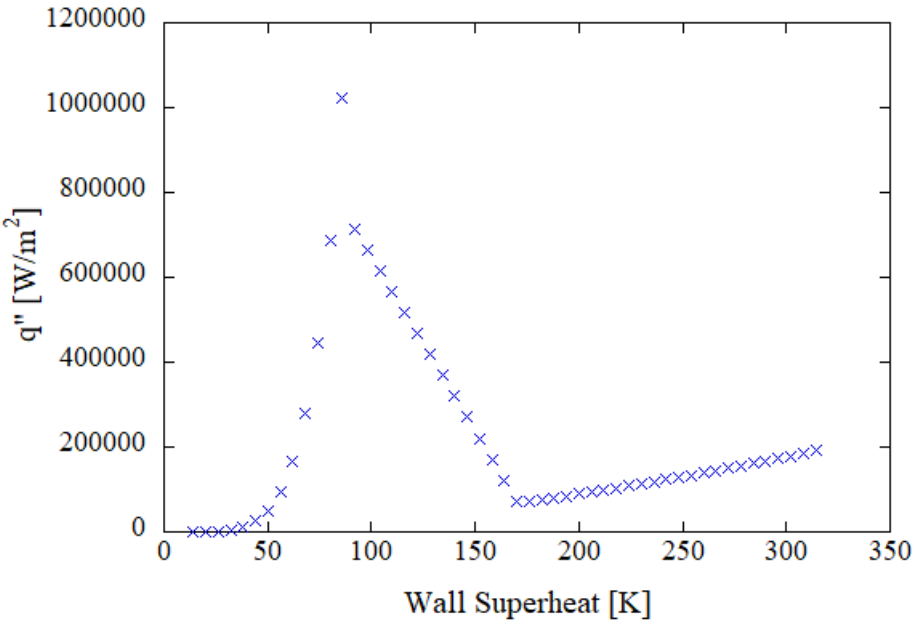

Figure 9: Third spray cooling correlation set used in evaluation.

As previously noted, two of the three correlation sets tested were developed using water as the working fluid. As a result, it is expected that some of the critical points along these boiling curves will be incorrect for the cryogenic fluids used in the model. While some research has been done on cryogenic propellant spray cooling, the figures reproduced using the correlations developed in those works did not yield reasonable boiling curves. For this reason, these correlations were not evaluated in this study. As new research becomes available related to the boiling heat transfer of

cryogenic spray, it should be tested and potentially incorporated to future versions of this model.

2.1.3 Additional Subroutine Considerations

In addition to the two-phase heat transfer correlations and the natural convection correlations, it was decided to check two additional parameters.

Droplet Heat Transfer

The first parameter which was tested was the correlation used to calculate the heat transfer coefficient for flow over a sphere. Since the droplets are assumed spherical for the sake of this model, this parameter is used to assess the heat transfer between the cryogenic propellant droplets and the ullage. The original droplet heat transfer correlation comes from Incropera [43] and is shown in Equation 2.13.

$$Nu = 2 + 0.6Re^{1/2}Pr^{1/3} \tag{2.13}$$

The alternative equation for heat transfer between a sphere and the surrounding flow comes from Whitaker [44]. Whitaker's correlation for the heat transfer caused by flow over a sphere is shown below.

$$Nu = 2 + \left(0.4Re^{1/2} + 0.06Re^{2/3}\right) Pr^{0.4} \left(\frac{\mu_v}{\mu_l}\right)^{1/4} \tag{2.14}$$

The obvious difference between the two different correlations is the inclusion of the fluid viscosity in the Whitaker correlation (Equation 2.14). Given the strong dependence of a fluid's viscosity on temperature and considering the sometimes large spans of temperature present in a given test, it was decided that it would be valuable to to consider this alternative in the evaluation.

Evaporation / Condensation at the Liquid-Vapor Interface

The second additional evaluation conducted was related to the equilibrium assumption present in the calculation of evaporation / condensation at the liquid-vapor interface. In a relatively quiescent system, this can be modeled by equating the heat transfer from the interface to the liquid with that from the gas to the interface as shown in Equation 2.15.

$$\dot{m}_{evap} = \frac{\dot{Q}_{il} - \dot{Q}_{gi}}{h_{fg}} \tag{2.15}$$

The resultant difference in heat transfer is simply divided by the latent heat of vaporization. This is possible because the interface is assumed to be infinitesimal and therefore unable to accumulate any mass or do any work.

Another well-known alternative to this approach was also tested, however. This alternative approach does not make an assumption of equilibrium but instead relies on molecular kinetic theory to describe the phase change present at a liquid-vapor interface. There are a number of variations on the equations used to describe this phenomena (typically called Hertz-Knudsen or Schrage equations) but for the sake of this correlation assessment, a relatively straightforward manifestation from Zhang et al [45] is used as shown in Equation 2.16.

$$\dot{m}_{evap} = \alpha\sqrt{\frac{M}{2\pi R}}\left[\frac{P_s(T_l)}{\sqrt{T_l}} - \frac{P_g}{\sqrt{T_g}}\right] \tag{2.16}$$

where M is the molar mass, R the universal gas constant, $P_s(T_l)$ the saturation pressure at the liquid temperature, and α the accommodation coefficient, which is determined empirically. The implementation of this new approach to calculate the evaporation rate at the interface was to simply replace Equation 2.15 with Equation 2.16 in the code itself. The value for α used in this work was 0.01. This is

based on work done by Kartuzova and Kassemi [46]. While other works to characterize accommodation coefficients for cryogenic propellants provided different ranges for accommodation coefficients, it was found during this study that the value of 0.01 performed best with respect to model convergence and stability. Future work could consider these different accommodation coefficients in conjunction with the broader correlation assessment. This may find correlation combinations that show more agreement with other works such as that by Bellur (2018) [47]. In that study, a range of values for α between 0.22 and 0.65 for H_2 was found. For a more detailed description of the kinetic theory modeling for evaporation / condensation and the associated calculation of accommodation coefficients, the reader is referred to works by Thomas and Olmer [48] and Bellur et al (2016) [49].

2.2 Testing Methodology

Given the large number of possible combinations that could be reviewed, it was decided to bound the number of correlations tested to three for both natural convection and spray cooling. Within natural convection, there is a further subsegmentation into natural convection between the ullage and the hot wall and the liquid-interface/gas-interface effects. For interfacial natural convection, only two correlations were modeled because after further inspection it was found that the heat transfer generated in the original interfacial natural convection correlations caused noticeable numerical instability in the revised version of the model. Therefore, a total of 18 correlation sets were tested in total. It was decided that this approach provided a reasonably broad assessment of different correlations without becoming too computationally and analytically expensive. The correlations which were chosen to be tested were done so based on their relevance to either cryogenic fluids, tank geometries, or broad industry acceptance. The 18 different correlation sets that were

tested are shown below in Table IV.

Table IV: Test matrix of modeled correlations

Correlation Set	Natural Convection	Spray Cooling	Interfacial Heat Trans.
1	Original Corr. (NC1)	Liang & Mudawar [32][33] (SC1)	Yang & West [17] and Guyer [22] (IFHT1)
2	Original Corr.	Liang & Mudawar [32][33]	McAdams [20] (IFHT2)
3	Original Corr.	Cryogen-Specific Corr. [34]–[39] (SC2)	Yang & West [17] and Guyer [22]
4	Original Corr.	Cryogen-Specific Corr. [34]–[39]	McAdams [20]
5	Original Corr.	Mudawar & Valentine [41] and Klingzing et al [42] (SC3)	Yang & West [17] and Guyer [22]
6	Original Corr.	Mudawar & Valentine [41] and Klingzing et al [42]	McAdams [20]
7	Yang & West [17] and Guyer [22] (NC2)	Liang & Mudawar [32][33]	Yang & West [17] and Guyer [22]
8	Yang & West [17] and Guyer [22]	Liang & Mudawar [32][33]	McAdams [20]
9	Yang & West [17] and Guyer [22]	Cryogen-Specific Corr. [34]–[39]	Yang & West [17] and Guyer [22]
10	Yang & West [17] and Guyer [22]	Cryogen-Specific Corr. [34]–[39]	McAdams [20]
11	Yang & West [17] and Guyer [22]	Mudawar & Valentine [41] and Klingzing et al [42]	Yang & West [17] and Guyer [22]
12	Yang & West [17] and Guyer [22]	Mudawar & Valentine [41] and Klingzing et al [42]	McAdams [20]
13	McAdams [20] (NC3)	Liang & Mudawar [32][33]	Yang & West [17] and Guyer [22]
14	McAdams [20]	Liang & Mudawar [32][33]	McAdams [20]
15	McAdams [20]	Cryogen-Specific Corr. [34]–[39]	Yang & West [17] and Guyer [22]
16	McAdams [20]	Cryogen-Specific Corr. [34]–[39]	McAdams [20]
17	McAdams [20]	Mudawar & Valentine [41] and Klingzing et al [42]	Yang & West [17] and Guyer [22]
18	McAdams [20]	Mudawar & Valentine [41] and Klingzing et al [42]	McAdams [20]

Following this initial determination of the best correlation set, a secondary evaluation was conducted. This secondary evaluation tested the alternative correlation for the droplet heat transfer subroutine as well as the different approach to modeling evaporation and condensation at the liquid-vapor interface as described in Section 2.1.3. This resulted in three more correlation sets being run, bringing the total to 21. The final three correlation sets were run using the 'winning' natural convection, spray cooling, and interfactial heat transfer correlations from Table IV. This baseline set of correlations used the Incropera [43] droplet heat transfer correlation (Equation 2.13) and the equilibrium assumptions for evaporation and condensation (Equation 2.15). These final correlation combinations are presented in Table V with

correlation set **a** being the original winning correlation set from Table IV.

Table V: Test matrix of secondary correlations

Correlation Set	**Droplet Heat Transfer**	**Evaporation / Condensation**
a	Incropera [43]	Equilibrium Assumption
b	Whitaker [44]	Equilibrium Assumption
c	Incropera [43]	Schrage Equation [45]
d	Whitaker [44]	Schrage Equation [45]

The ultimate goal of this correlation evaluation was to find which combination of correlations resulted in the best prediction compared to experimental data. To ensure even coverage across a broad range of experimental conditions, each model was tested on 34 different experiments. In addition to the two experiments that this work presents, it was decided to include four other experiments in the overall correlation assessment. These four experiments and the specific model results will not be presented in this paper but will become the subject of their own work at a later date. A high level overview of these additional tests are presented in Table VI, along with the two previously mentioned experiments that will be covered in the following chapters. The experiments which are covered in this work are bolded. Table VI also lists sources (where available) for additional context on all experiments analyzed.

Table VI: Overview of cases used for correlation evaluation

Experimental Set	**# of Cases**	**Cryogen**	**Tank Geometry**	**Tank Material**	**Injection Method(s)**	**NVF / NVTO**
Chato 1991 [12]	9	LH2	Domed Cylinder	2219 Aluminum	Top Spray, Bottom Spray	NVF
Chato and Sanabria [50]	1	LH2	Domed Cylinder	2219 Aluminum	Top and Bottom Spray	NVF
CRYOTE 2 [51]	14	LN2	Spherical	304 Stainless Steel (lid), Titanium 6-4 (body)	Top and Bottom Spray	NVTO
MSFC Advanced Shuttle Upper Stage [52]	7	LH2	Domed Cylinder	5083 Aluminum	Spray Bar	NVTO
CRYOTE 1	1	LN2	Spherical	304 Stainless Steel (lid), Titanium 6-4 (body)	Top Spray	NVTO
GRC Flightweight Tank	2	LH2	Domed Cylinder	2219 Aluminum	Spray Bar	NVTO

To evaluate the accuracy of the model compared to the experimental data, Mean Absolute Error, MAE, and Mean Absolute Percentage Error, $MAPE$, were calculated according to the expressions given in Equation 2.17.

$$MAE = \frac{\sum_{i=1}^{n} \mid y_i - x_i \mid}{n} \quad \text{and} \quad MAPE = \frac{1}{n} \sum_{i=1}^{n} \left| \frac{y_i - x_i}{x_i} \right| \tag{2.17}$$

where y_i represents the model prediction at a given timestep and x_i the corresponding experimental value at the same timestep.

For each experiment, it was necessary to ensure that the proper values were compared for the MAE and MAPE calculation. In most cases, the model timestep was finer than that of the experimental data. The timestep for the model was set to $0.01s$ while most experimental data was reported in $0.05s$ increments. In these cases, the experimental value was compared to the model value at the same timestep e.g., experimental data at $2.35s$ was compared to model data at $2.35s$. Model results at $2.34s$ and $2.36s$ were not used in the performance evaluation.

For all cases, the MAE and $MAPE$ were calculated for the RT pressure. When available, other parameters such as fill percentage, two-phase node temperature, wall-gas node temperature, liquid mass, and gas mass were also tracked and compared against model outputs. For the sake of the correlation evaluation, pressure is the primary metric used to assess model performance. This is not only because it is available for all of the experimental cases but also because it is a primary design and safety criteria that this model will be used to help evaluate for future experiment design. To account for other variables, it was decided to create a composite score. The weights used to determine the composite score were chosen by the author and colleagues based on our assessment of a variable's relative importance. The composite score was comprised of pressure MAPE, fill percentage MAPE, T_{wg} MAPE, and T_{tp} MAPE. The weightings were 50%, 30%, 10%, and 10% respectively. The values of MAPE used in the composite score were the mean variable values across all cases in a given correlation set e.g., T_{wg} MAPE for all cases run in correlation set 1 were averaged to be used in the composite score.

2.3 Results

Following approximately 2000 hours of compute time, it was found that the best performing correlation set based upon the composite score described in the previous section was number 13 from Table IV. The full results can be seen in Figure 10. In addition to the composite score, Figure 10 also shows the ranked performance of the different correlation sets based on a given variable.

Rank	*Composite Score*	*Pressure*	*Fill*	T_{wg}	T_{tp}
1	13	13	13	5	9
2	17	17	17	3	7
3	6	4	8	13	11
4	5	6	6	7	8
5	4	15	7	6	10
6	8	3	5	17	5
7	3	5	14	4	4
8	7	10	18	15	3
9	15	8	4	11	6
10	10	9	3	9	13
11	9	7	11	8	17
12	11	11	10	14	15
13	14	14	9	18	18
14	18	18	15	10	14
15	16	16	16	16	16
16	1	1	2	1	12
17	2	2	1	2	1
18	12	12	12	12	2

Figure 10: Ranking of correlation set performance based on different variables of interest

As expected, correlation set 13 also performs best with respect to pressure and fill MAPE, leading to a favorable composite score. Alternatively, correlation sets 5 and 9, which performed the best for T_{wg} and T_{tp}, respectively, had a worse composite score because temperature was chosen to be a relatively less important parameter.

The mean and standard deviation of the error rates calculated for all cases run using correlation set 13 are shown in Table VII.

Table VII: Summary of error rates calculated for cases run using correlation set 13.

Variable	**Mean**	**Std. Dev.**
Pressure	0.266	0.231
Fill %	0.412	0.388
T_{wg}	0.293	0.427
T_{tp}	0.247	0.351

As shown in Table VII, the standard deviation relative to the mean is quite high. This suggests a relatively decentralized distribution across the different in-

spection variables. This is somewhat evident in Figure 11 where one can see the interquartile range (i.e., 50% of the data) of the boxes extends well beyond the median values. Another interesting note regarding Figure 11 is that there appears to be a consistent right skewness to the distributions, evidenced by the long 'whisker' in the positive direction. These non-Gaussian distributions were considered when thinking about what statistics to report in this analysis but ultimately it was decided to report the mean over the median since this is commonly how model performance is presented in the literature.

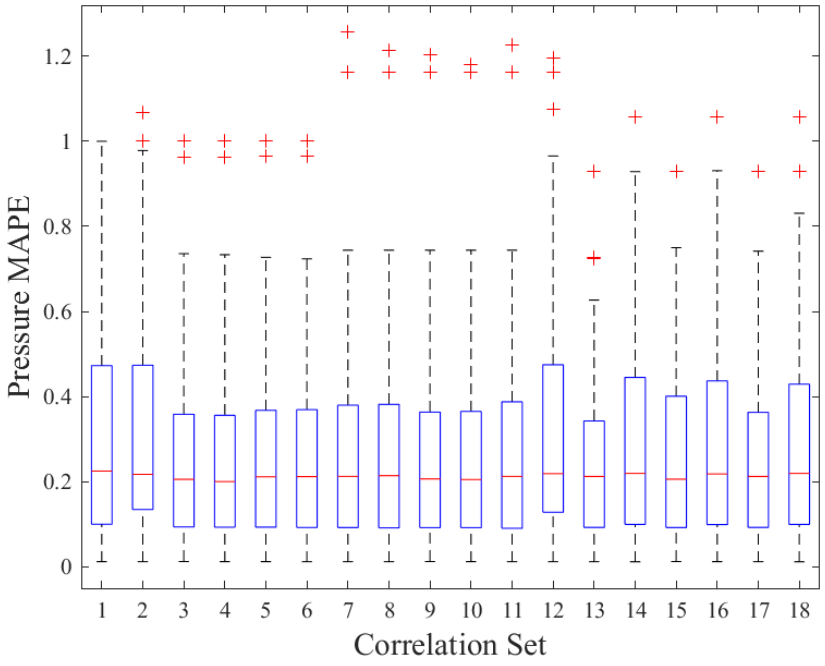

Figure 11: Box and whisker plot of pressure MAPE across all cases tested using the different correlation sets.

To better show the pressure predictive performance of the different correlation sets compared with one another, Figure 12 was produced. This figure shows a clear distinction in performance between the different sets. For example, the winning correlation set (13) shows a 29% improvement over the poorest performing set (12) which had an average pressure MAPE across all cases of 37.5%. In comparison,

correlation set 13 had an average pressure error of 26.6% across all cases.

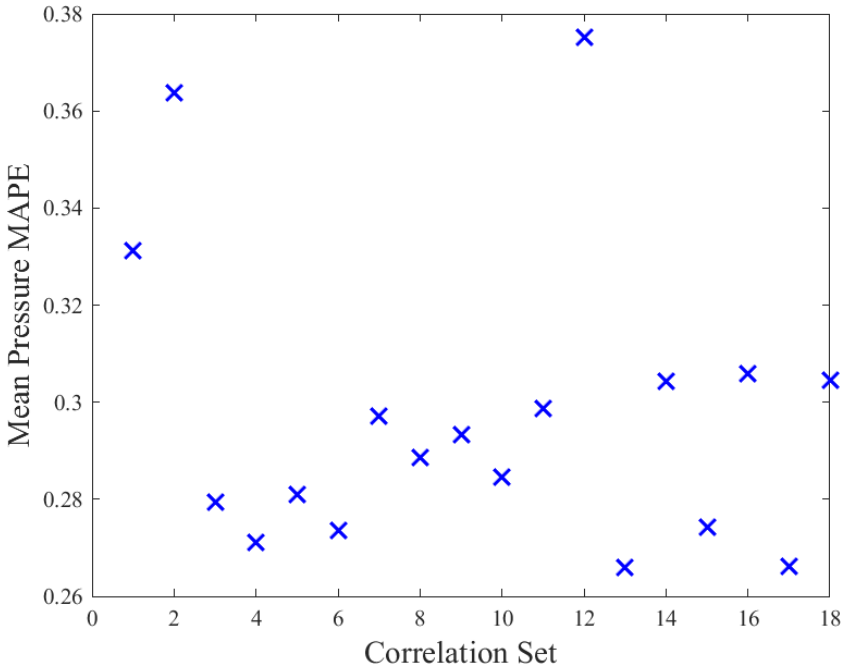

Figure 12: Mean pressure MAPE by correlation set.

In addition to performing the best overall, correlation set 13 also performed the best for the hydrogen-specific cases as shown in Figure 13. For LN2 cases, however, the best performing correlation set was 18. The difference between these two correlation sets is the spray cooling and interfacial heat transfer correlations. Both correlation set 13 and 18 use correlations developed in part by Mudawar [32] [33] [41] but the film boiling region of the curve used in 18 was developed by Klingzing [42]. As can be seen when comparing figures 7 and 9, the boiling curves are very similar to each other. One possible explanation is the change in film boiling correlation. Given the fact that LH2 spends a significant amount of time in film boiling, as compared to LN2, due to its relatively much lower Leidenfrost temperature, it's possible that the film boiling correlations developed in Liang and Mudawar's work [32] [33] better represents LH2 film boiling as compared to Klingzing's correlation. Another difference between correlation set 13 and 18 is the set of correlations used to model natural convection at

the liquid-vapor interface. Correlation set 13 uses equations developed by Yang and West [17] and Guyer [22] whereas correlation set 18 uses equations from McAdams [20]. Given that Yang and West's correlations were developed based on cryogenic fluids, it is unsurprising that they performed better with LH2 than those of McAdams, which are more generic in nature.

Rank	*All Cases*	*LH_2 Cases*	*LN_2 Cases*
1	13	13	18
2	17	17	14
3	6	4	6
4	5	6	12
5	4	5	2
6	8	15	8
7	3	3	13
8	7	8	5
9	15	10	11
10	10	7	7
11	9	9	1
12	11	11	17
13	14	14	4
14	18	18	3
15	16	16	10
16	1	1	9
17	2	2	15
18	12	12	16

Figure 13: Ranking of correlation set performance segmented by cryogen.

The final analysis conducted on the main correlation assessment attempted to understand the sensitivity of the model output to changes in the different correlation sets. Figure 14 is an attempt to quantify this sensitivity. While more rigorous sensitivity analyses are left to other authors interested in the subject, the analysis in Figure 14 seeks to quantify the incremental benefit / detriment of a given correlation in comparison with another. To understand the analysis in Figure 14, the percentages represent the relative performance of variable a to that of variable b e.g., SC1 performed approximately 3.3% worse than SC2 overall, though for correlation set 13 it performed 5.3% better. Finally, the actual correlations are represented by the shorthand presented in Table IV for readability and concision.

Corr. Set	*Composite Score*	*Natural Convection*	*Spray Cooling*	*Interfacial Heat Trans*	*SC1 vs SC2*	*SC1 vs SC3*	*SC2 vs SC3*	*IFHT1 vs IFHT2*	*NC1 vs NC2*	*NC1 vs NC3*	*NC2 vs NC3*
13	0.310	NC 3	SC 1	IFHT 1	5.3%	0.3%	--	8.0%	--	--	--
17	0.311	NC 3	SC 3	IFHT 1	--	--	--	7.8%	--	--	--
6	0.315	NC 1	SC 3	IFHT 2	--	--	--	--	27.1%	6.5%	--
5	0.319	NC 1	SC 3	IFHT 1	--	--	--	-1.0%	4.8%	-2.2%	--
4	0.319	NC 1	SC 2	IFHT 2	--	--	-1.3%		2.8%	8.0%	--
8	0.321	NC 2	SC 1	IFHT 2	2.3%	24.9%	--	--	--	--	4.4%
3	0.323	NC 1	SC 2	IFHT 1	--	--	-1.5%	-1.2%	2.4%	1.1%	
7	0.325	NC 2	SC 1	IFHT 1	1.8%	2.6%		-1.3%	--	--	-4.6%
15	0.327	NC 3	SC 2	IFHT 1	--	--	-4.7%	5.6%	--	--	--
10	0.328	NC 2	SC 2	IFHT 2	--	--	22.1%	--	--	--	5.1%
9	0.331	NC 2	SC 2	IFHT 1	--	--	0.8%	-0.8%	--	--	-1.3%
11	0.334	NC 2	SC 3	IFHT 1	--	--	--	20.1%	--	--	-6.7%
14	0.335	NC 3	SC 1	IFHT 2	3.0%	0.2%	--	--	--	--	--
18	0.336	NC 3	SC 3	IFHT 2	--	--	--	--	--	--	--
16	0.345	NC 3	SC 2	IFHT 2	--	--	-2.7%	--	--	--	--
1	0.375	NC 1	SC 1	IFHT 1	-13.7%	-15.0%	--	4.8%	-15.2%	-17.2%	--
2	0.393	NC 1	SC 1	IFHT 2	-18.6%	-19.7%	--	--	-18.2%	-14.6%	--
12	0.401	NC 2	SC 3	IFHT 2	--	--	--	--	--	--	-16.3%
				Average Performance Difference	**-3.3%**	**-1.1%**	**2.1%**	**4.7%**	**0.6%**	**-3.1%**	**-3.2%**

Figure 14: Comparison of correlation impact on model performance.

Somewhat counterintuitively, the correlations which comprise correlation set 13 do not all have the highest average benefit on model output in their respective category. This is almost certainly due to the myriad coupled interactions among the different correlations. It is interesting to note, however, that correlation set 13 is composed of 2 of the 3 best performing correlations in their category. Specifically, NC3 performs the best of the natural convection correlations and IFHT2 performs better than IFHT3 on average.

Having completed the initial correlation assessment, the next step was to assess the impact of the alternative droplet heat transfer correlation and the non-equilibrium assumption at the liquid-vapor interface as described in Table V. The results of this analysis are shown below in Figure 15.

	Correlation Set			
	13a (orig.)	**13b**	**13c**	**13d**
Comp. Score	0.310	0.362	0.303	0.355
Pressure MAPE	0.266	0.394	0.259	0.384
Fill MAPE	0.412	0.366	0.396	0.352
T_{wg} MAPE	0.293	0.318	0.295	0.326
T_{tp} MAPE	0.247	0.238	0.249	0.246

Figure 15: Secondary correlation assessment results.

The results presented in Figure 15 suggest that the original correlation set with the revised droplet heat transfer correlation from Whitaker [44] performs the best overall. Additionally, it is worth noting that while the non-equilibrium cases performed worse overall than the equilibrium cases, their fill prediction performance was better. This may be because of the an improvement in the evaporation / condensation mass flow rate. Future studies could conduct a more broad correlation assessment which would incorporate the equilibrium / non-equilibrium assumption in the original assessment. This would significantly increase compute time but may lead to a final result with both improved pressure and fill prediction performance. Given the results shown in Figure 15, all model plots produced in later chapters will be done using correlation set 13c.

CHAPTER III

CRYOTE 2 Experiments

3.1 Experimental Description

While a brief description of the experimental setup and test facility is presented here for context, the reader is referred to Hartwig et al. (2021) [51] for a more thorough description of the CRYOTE-2 tests. Between 2014 and 2016, 53 experiments were conducted using the CRYOTE-2 setup. These tests were conducted using LN2 with a spherical RT comprised of a thin walled 6-4 titanium tank with a 304 stainless steel lid. The tank had an OD of 75.44 cm and a wall thickness of 0.127 cm. The lid was a 0.952 cm thick cylindrical section that was 20.32 cm in diameter. Given its composition and relatively higher thickness, the lid was disproportionately more massive than the tank wall. The tank itself had a mass of approximately 9.84 kg while the lid alone weighed an additional 2.47 kg. The internal volume of the tank at room temperature was 0.222 m3. As shown in Figure 16 [53] [54], the spherical CRYOTE tank was housed within a larger vacuum chamber. This vacuum chamber, known as the Exploration Systems Test Facility (ESTF), is a multi-purpose test chamber located at NASA's Marshall Space Flight Center. The ESTF is 6.1 m long and 2.74 m in diameter. Also located inside the ESTF is the Vibro-Acoustic Test Article (VATA) tank which served as the supply tank for these tests. VATA is a vertically oriented domed tank constructed of stainless steel. For these tests, VATA is insulated

using multi-layer insulation (MLI) as well as a broad area cooling shield.

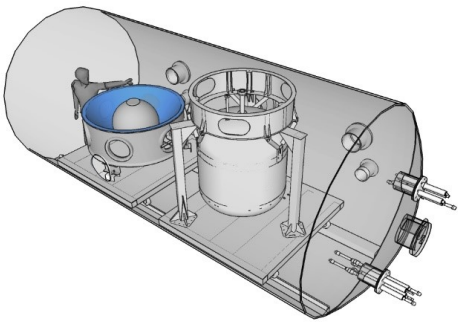

Figure 16: CRYogenic Orbital TEst bed (CRYOTE) 2 tank (left) inside the Exploration Systems Test Facility. The Vibro-Acoustic Test Article tank is located on the right.

To inject the LN2 into the CRYOTE tank, three different injectors were used. The injectors used were optimized for different chilldown modes. The first injector sprayed the LN2 upwards at the relatively thick lid. As shown in Figure 17a, this injector produced relatively large droplets intended to cool down the lid via boiling. All of the spray that did not boil from this 16-hole injector was assumed to wash down the walls. The second injector used was an adaptation on the first wherein 8 of the 16 holes were blocked. Then a 170° BETE TF10 spray nozzle was attached to the bottom of the inverted spray injector. The spray pattern of this second injector can be seen in Figure 17b. The spray produced in this case consisted of relatively large droplets directed at the lid, similar to the first injector, as well as a finer mist directed into the ullage of the tank. This finer mist was intended to aid in the condensation of ullage vapor, thus reducing overall tank pressure. The third and final injector used was a three-spray system which used commercial nozzles. As seen in Figure 17c, one nozzle is directed upwards at the lid and two are directed down into the tank. The upward-facing nozzle is a 170° BETE TF8 nozzle while the two downwards facing nozzles are both 170° spray angle nozzles from BETE, one being a TF10 and the other a TF6.

Compared to the other injectors, this injector atomizes the spray significantly more which likely reduces the boiling at the wall and increases the ullage cooling potential. Based on analysis described in Hartwig et al's work, 32.5% of the spray is directed upwards, 50% is directed downwards in the center TF10 nozzle, and the remaining 17.5% is passed through the TF6 nozzle (on the right in Figure 17c).

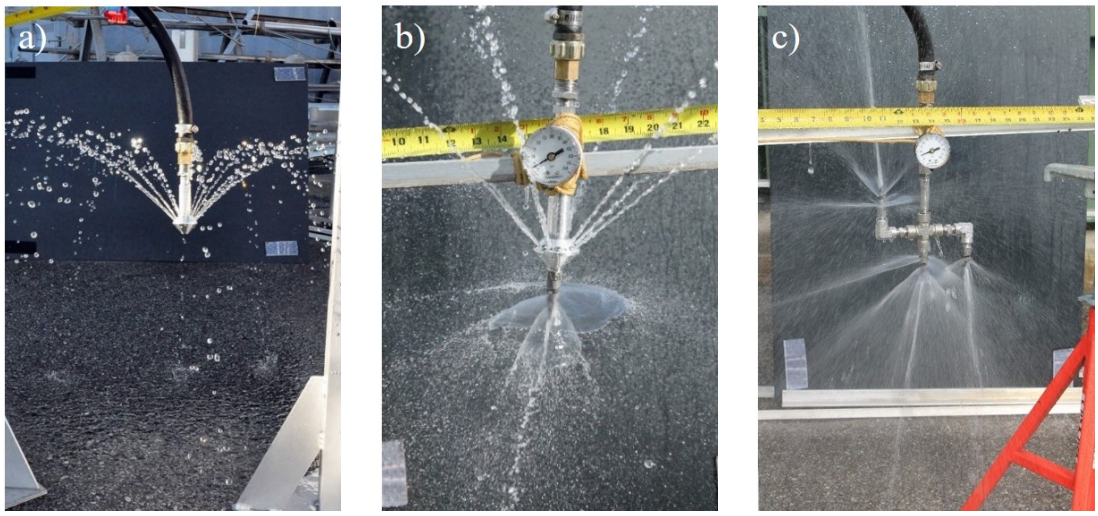

Figure 17: Injectors used in the CRYOTE 2 experiments. (a) is the 16-hole Inverted Spray, (b) the 8-hole Inverted and Downward Spray Cone and (c) the 3 Nozzle Injector

Due to the long span during which the CRYOTE-2 experiments occurred, the exact instrumentation fluctuated somewhat. In general, however, Figure 18 shows the location of the critical thermocouples (TCs) present on the RT. As will be described more thoroughly in following sections, these TCs are used to help define both the initial state of the tank and the time-series temperature response of the system during NVF/NVTO. In addition to the instrumentation present on the RT, sensor data from the supply tank and transfer line was equally critical to defining the necessary modeling parameters. These sensors are described in Figure 19. Additionally, more information for the RT sensors is provided in Figure 20.

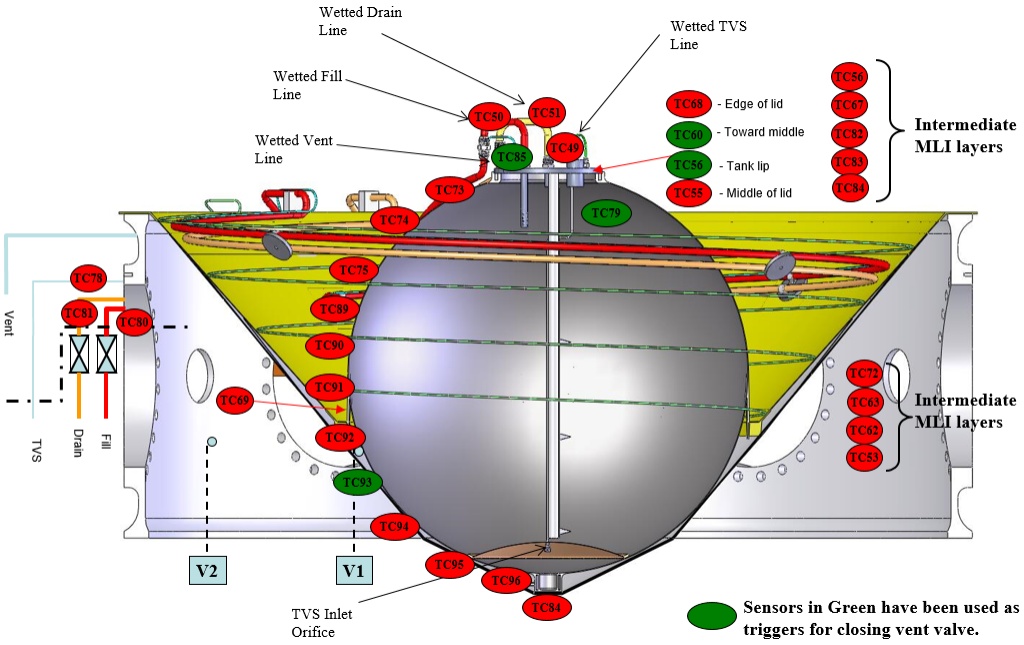

Figure 18: CRYOTE 2 thermocouple location

VATA Sensors		
Thermocouple Location Description	**DAQ ID**	**Units**
Tank Surface Bottom	SD008	K
VATA Load Cells	**DAQ ID**	**Units**
Load Cell 1	SG001	lbs
Load Cell 2	SG002	lbs
Load Cell 3	SG003	lbs
VATA Pressure Transducers	**DAQ ID**	**Units**
VATA Ullage Pressure	D-PT-V616	PSIA

Figure 19: Supply tank sensor descriptions

CRYOTE Sensors					
Thermocouple Location Description	**DAQ ID**	**Uncertainty**	**Thermocouple Location Description**	**DAQ ID**	**Uncertainty**
Wetted thru TVS tee at Lid ~ 39.5% fill level	TC49	+/- 2 degrees K	Transfer line TC, 47" from TC 86 (right before Valve Z)	TC87	+/- 2 degrees K
Wetted Fill at Lid	TC50	+/- 2 degrees K	Transfer line TC, 16" from TC 87 (right before tee with CRYOTE drain line)	TC88	+/- 2 degrees K
On skirt inside turn 1 from tank	TC52	+/- 2 degrees K	71.9% fill level, external to tank	TC89	+/- 2 degrees K
On skirt inside turn 4 from tank	TC54	+/- 2 degrees K	57.5% fill level, external to tank	TC90	+/- 2 degrees K
Close to center of lid	TC55	+/- 2 degrees K	42.5% fill level, external to tank	TC91	+/- 2 degrees K
CRYOTE tank lip (at lid but on main tank body)	TC56	+/- 2 degrees K	28.1% fill level, external to tank	TC92	+/- 2 degrees K
On skirt inside turn 2 from tank	TC57	+/- 2 degrees K	15.5% fill level, external to tank	TC93	+/- 2 degrees K
On skirt inside turn 5 from tank	TC58	+/- 2 degrees K	6.0% fill level, external to tank	TC94	+/- 2 degrees K
Tank Lid, half way between edge and center of lid	TC60	+/- 2 degrees K	0.7% fill level, external to tank	TC95	+/- 2 degrees K
TVS turn 5 from tank	TC61	+/- 2 degrees K	0.0% fill level, external to tank	TC96	+/- 2 degrees K
on skirt inside turn 3 from tank	TC64	+/- 2 degrees K			
TVS turn 3 from tank	TC65	+/- 2 degrees K			
TVS turn 4 from tank	TC66	+/- 2 degrees K	**Cryote Load Cells**	**DAQ ID**	
Edge of Tank Lid, thicker part	TC68	+/- 2 degrees K	Load Cell 4	SG004	unknown
TVS turn 2 from tank	TC70	+/- 2 degrees K	Load Cell 5	SG005	unknown
99.3% Fill level, external to tank	TC73	+/- 2 degrees K	Load Cell 6	SG006	unknown
94.0% fill level, external to tank	TC74	+/- 2 degrees K			
84.4% fill level, external to tank	TC75	+/- 2 degrees K	**Pressure Transducers**	**DAQ ID**	
CRYOTE Wetted 95% fill level	TC79	+/- 2 degrees K	Pressure upstream of Spray Head	AI50	+/- 0.5% BFSL
tank fill line at ESPA ring	TC80	+/- 2 degrees K	Pressure TVS Vent Line at HX	AI51	+/- 0.5% BFSL
Temp CRYOTE Spray	TC82	+/- 2 degrees K	Pressure CRYOTE2 ullage tap (dedicated)	AI52	+/- 0.5% BFSL
Temp TVS Vent at HX	TC83	+/- 2 degrees K	Pressure TVS Flowmeter	AI53	+/- 0.5% BFSL
Tank sump at base of cup (Very bottom of tank)	TC84	+/- 2 degrees K			
Wetted Vent at Lid	TC85	+/- 2 degrees K	**Flow Meters**	**DAQ ID**	
Transfer line TC, 60" from VATA TC36	TC86	+/- 2 degrees K	TVS Volumetric Flow Meter	FM-T362	unknown

Figure 20: Receiver tank sensor descriptions

3.2 Model Inputs / Considerations

While the generalized UNVF model was capable of handling the majority of the necessary geometry, propellant, and other test-specific conditions without modification, it was necessary to make some accommodations for the injectors used in the CRYOTE-2 experiment. Two of the three injectors used in these experiments leveraged commercially available nozzles which have well documented datasheets associated with them. For these injectors, manufacturer-defined relationships of Sauter-mean diameter versus pressure drop were used instead of the correlations described in the UNVF model overview paper. These relationships made it possible to estimate the droplet size as it left the injector as a function of the pressure difference between the supply and RT pressures.

In addition to the accommodation made for the CRYOTE-2 injectors, it was

also necessary to adjust the model to be able to handle both materials used in the RT. Given how the trajectory code of the model defines the wall-gas / two-phase / liquid boundaries, it would have been necessary to define a new 'lid node' which would itself have to be possibly split into two-phase, wall-gas, or liquid nodes depending upon the injector being used and the liquid level in the tank. This capability would have resulted in significant modification to the structure of the model and its method of solution. As a result, it was chosen to use Kopp's Law and define the material properties on a mass-averaged basis. While Kopp's Law is traditionally applied to specific heat, it was decided to use the same mass-averaging scheme for the tank's thermal conductivity as well due to the aforementioned challenges associated with defining new nodes in the UNVF model. Figures 21a and 21b show the effect of using the mass-average to define the tank's specific heat and thermal conductivity. Based on the lid and tank masses, a weight of 80% was applied to the titanium tank wall properties and the remaining 20% was applied to the stainless steel lid properties. For the UNVF model, specific heat and thermal conductivity parameterizations were obtained from Marquardt et al [55] and the Titanium Metals Corporation [56].

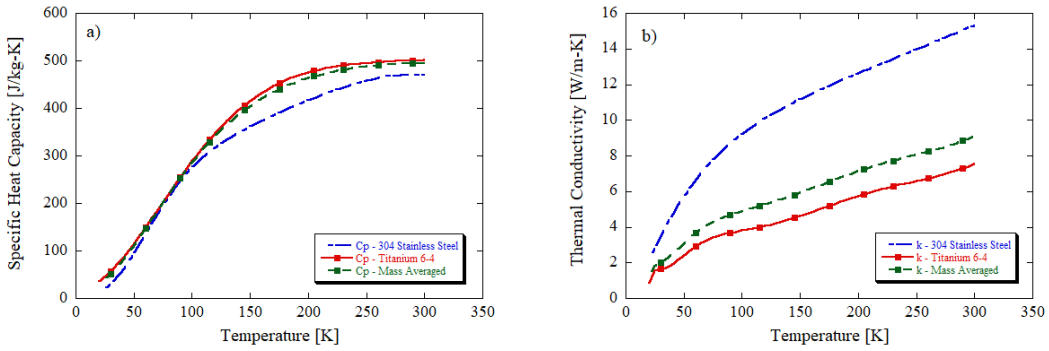

Figure 21: Effect of mass-averaging on (a) specific heat and (b) thermal conductivity for CRYOTE 2 receiver tank.

The final adjustment that was made to the UNVF code to model the CRYOTE-

2 tests was related to the trajectory of the propellant itself. As described in the UNVF model paper, the model can accommodate multiple injection methods. To model the bi-directional injectors in the CRYOTE-2 tests, the pre-existing injection methods were combined. The control volumes associated with the CRYOTE-2 injectors are reproduced in Figure 22 for completeness. It is assumed for the upward-spraying injectors that the spray that hits the wall then washes down, rather than bouncing off. This is reflected in the large two-phase node along the tank walls. The upward-spraying cone injector is modeled as a hollow cone based on the spray pattern shown in Figures 22a and 22b. This results in a small vapor/wall node at the top of the tank directly above the injector. For the three-nozzle injector, the upward-spraying nozzle is modeled as a full cone nozzle. Additionally, because the whole wall is a two-phase node for the three-nozzle injector, the horizontal displacement of the nozzle away from the vertical centerline of the tank does not have to be considered when calculating spray trajectory.

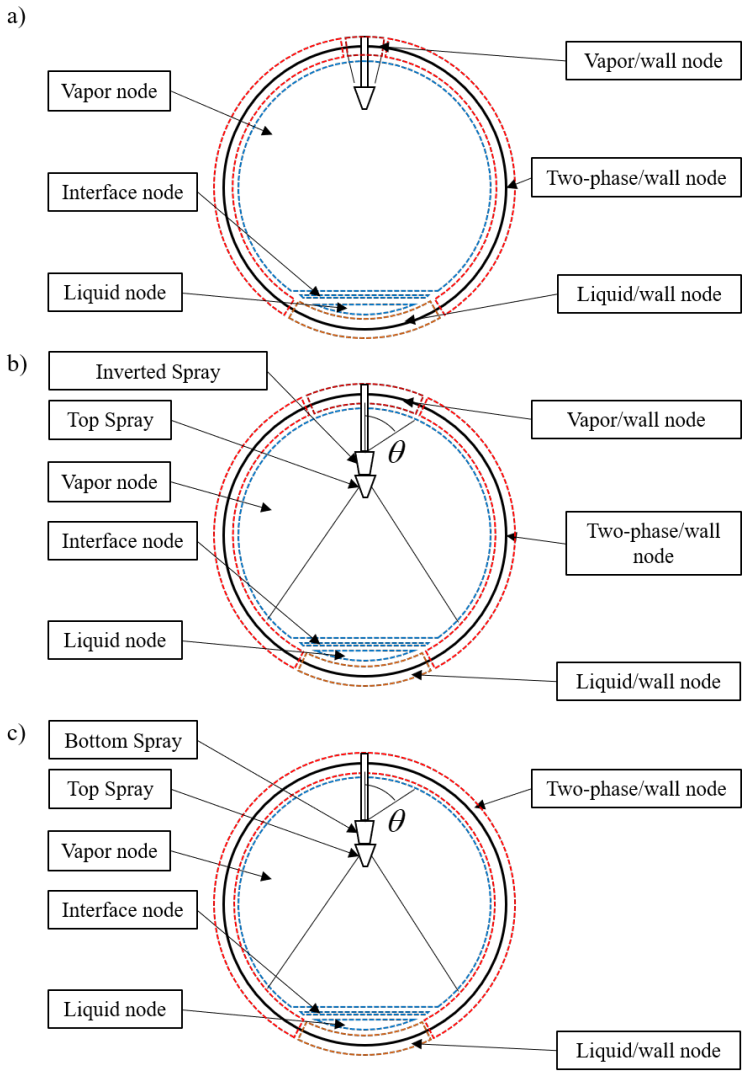

Figure 22: Model control volumes for the (a) 16-hole Inverted Spray, (b) 8-hole Inverted and Downward Spray Cone, and (c) 3 Nozzle injectors used in the CRYOTE 2 experiments

In order to appropriately define the inlet conditions for each experiment and then subsequently compare model outputs with the experimental results, it was necessary to adequately assess the relevant sensor data tied to the supply and receiver tanks. What follows is a brief description of the sensors used and the associated calculations needed to provide all necessary input and output values.

1. Receiver tank pressure: Specified by PT-T364 (for tests before 2016) and AI52 (for tests after 2016).

2. Fill level: Calculated by dividing the volume of the liquid in the tank by the total tank volume at any point in time, ignoring the small volume change as the tank contracts with colder temperature:

$$Liquid\ Level = \frac{V_{liquid}}{V_{tank}} = \frac{m_{liquid}}{\rho_{liquid} V_{tank}} = \frac{(m_{LC} - m_{CRYOTE}) - \rho_{vapor} V_{tank}}{\rho_{liquid} V_{tank} - \rho_{vapor} V_{tank}} \quad (3.1)$$

3. Mass flow rate: Calculated using conservation of mass and a volume constraint:

$$m_{load\,cell} - m_{CRYOTE} = m_{liquid} + m_{vapor} \quad (3.2)$$

$$V_{CRYOTE} = V_{liquid} + V_{vapor} \quad (3.3)$$

where m_{CRYOTE} is the mass of the empty receiver tank and m_{LC} is the mass reading from the load cell. Substituting the known liquid and vapor densities using REFPROP, Equation 3.3 becomes:

$$V_{CRYOTE} = \frac{m_{liquid}}{\rho_{liquid}} + \frac{m_{vapor}}{\rho_{vapor}} \quad (3.4)$$

Rearranging Equations 3.2 and 3.4 gives the set of two equations and two unknowns for vapor and liquid masses at any moment in time:

$$m_{vapor} = \frac{V_{tank} + \frac{m_{CRYOTE} - m_{LC}}{\rho_{liquid}}}{\frac{1}{\rho_{vapor}} - \frac{1}{\rho_{liquid}}} \quad (3.5)$$

$$m_{liquid} = m_{LC} - m_{CRYOTE} - m_{vapor} \quad (3.6)$$

4. Wall temperature readings:

   (a) Mass averaged tank temp at NVF start was calculated by taking a mass average of the lid and tank walls. Lid temperatures are given by thermocouples TC55, TC60, and TC68 and the main body temperatures are given by TC89-96 and TC73-75.

(b) TC79 is compared to T_{wg}.

(c) TC49 is compared to T_{tp}.

5. Inlet state:

   (a) For inlet pressure:

      i. For 2016 tests, AI50 measured pressure.

      ii. For successful tests, 20150218, 20150227, 20150303, 20150304.2, and 20150309.2, the pressure drop model from the Hartwig et al [51] paper was used.

      iii. For all other tests, inlet can be assumed saturated liquid using the median value of TC50.

   (b) TC50 is used to define the inlet temperature.

It was also necessary to define some test-specific assumptions to make it feasible to model the CRYOTE 2 cases:

1. The 16 hole injector sits 7.62 cm (3 in) from the lid and is therefore submerged at 96% fill.

2. 8-hole orifice

   (a) Top spray component of injector is submerged at 94% fill level.

   (b) Inverted top spray component of injector is submerged at 97% fill level.

3. 3-spray injector

   (a) Downward spray component of injector is submerged at 95% fill level.

   (b) Upward spray component of injector is submerged at 98% fill level.

4. The temperature of the vapor in the receiver tank is defined as the average value of TC49 and TC79.

5. The temperature of the liquid in the receiver tank is specified by TC50.

6. The thermodynamic state of the vapor in receiver tank is defined using average of TC49 and TC79, and the ullage pressure previously described.

7. The thermodynamic state of the liquid in receiver tank is defined using TC50 and the ullage pressure previously described. Note: hydrostatic pressure is assumed to be negligible.

8. In instances where the supply pressure was less than the saturation pressure based on the supply temperature, the saturation pressure was used instead in order to ensure single phase liquid at the inlet. This was done to avoid downstream REFPROP errors resulting from two-phase inlet states while still being able to accommodate inlet subcooling. An example of this is shown in Figure 23a.

9. Due to noise present in the inlet mass flow rate data, the data was smoothed using a simple moving average. This was calculated by averaging data 5 seconds before and 5 seconds after the data point under analysis. The effect of this smoothing is shown in Figure 23b for test 20161006.1 as an example. The purpose of this smoothing was to reduce additional noise input into the model to aid in convergence.

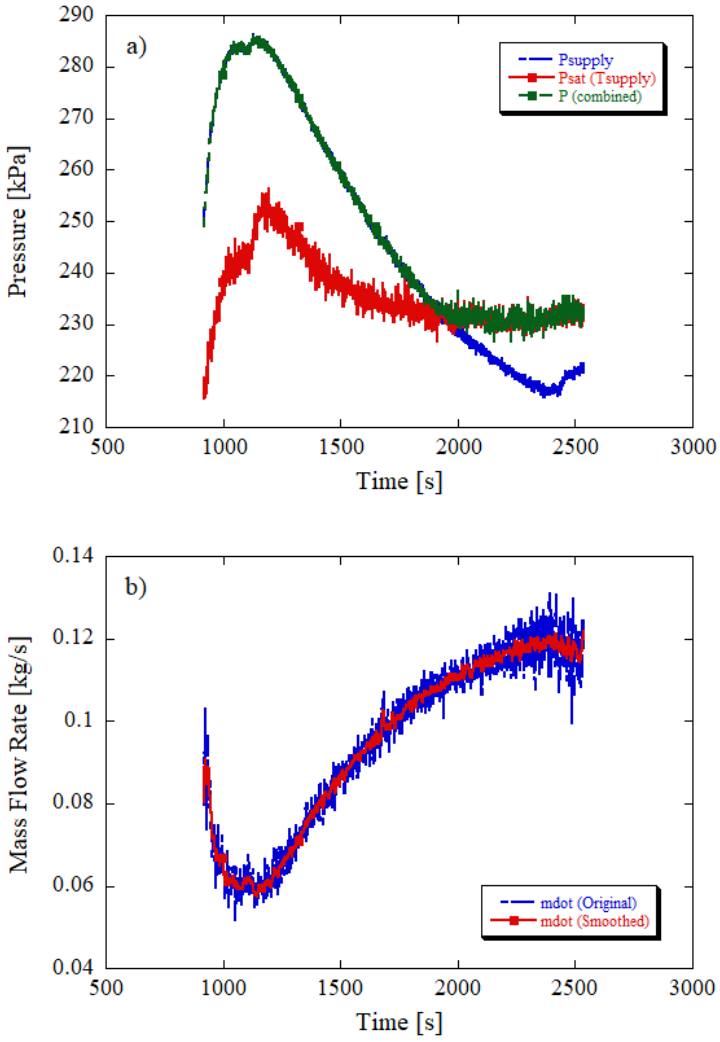

Figure 23: CRYOTE 2 model inlet condition management for (a) supply pressure and (b) mass flow rate.

The list of initial conditions input into the model are shown below in Table VIII.

Table VIII: CRYOTE 2 model initial conditions

Test	**Test Dur.**	T_{supply}	P_{supply}	**Avg.** $\dot{m}$	**RT** P **at NVF Start**	**RT Wall Temp at NVF Start**	**RT Vapor Temp at NVF Start**	**RT Liquid Temp at NVF Start**	m_g **at NVF Start**	m_l **at NVF Start**	**Initial Fill Level**	**Final Fill Level**
#	s	K	kPa	kg/s	kPa	K	K	K	kg	kg	%	%
20150218	866	83.69	265.19	0.19	160.21	90.74	109.56	81.46	1.19	1.83	1.06	94.6
20150227*	989	84.11	300.02	0.16	235.37	88.81	117.44	85.29	1.69	1.73	1.00	95
20150303	981	83.66	217.92	0.16	136.71	102.05	84.94	79.99	1.04	8.28	4.78	96.1
20150304.2	1201	84.08	256.11	0.13	140.68	162.15	151.11	80.25	0.67	0.96	0.56	94.3
20150309.2	1153	85.1	284.15	0.11	143.97	170.81	162.77	80.46	0.64	0.73	0.43	75.8
20160914*	24	85.88	288.83	0.03	261.53	90.85	86.75	86.75	2.19	1.42	0.83	1.1
20160921	1735	85.53	245.65	0.09	226.4	88.74	84.96	84.96	1.92	2.77	1.62	89.7
20161004*	33	86.58	277.02	0.06	244.28	89.77	86.20	86.20	2.05	2.28	1.34	2.3
20161005	1479	85.1	236.56	0.10	225.30	88.81	85.15	85.15	1.86	7.44	4.32	91.8
20161006.1	1622	85.21	243.45	0.09	233.50	89.23	85.64	85.64	1.92	6.77	3.94	94.1
20161006.2	1634	85.21	242.86	0.09	233.50	89.23	85.64	85.64	1.92	6.77	3.94	94.9
20161006.3	144	86.08	293.05	0.05	241.34	89.62	85.96	85.95	2.00	5.35	3.11	6.9
20161007*	700	88.77	302.87	0.03	235.85	89.41	85.71	85.71	1.95	6.17	3.59	16.3
20161012*	111	86.49	291.89	0.04	245.70	89.78	86.21	86.21	2.03	5.42	3.16	5.8

3.3 Results

Given the large number of experiments that were performed over the two-year span, it was desirable to pare down the number of cases presented. In this section, only a selected set of tests are presented. These specific cases were chosen in order to take advantage of the somewhat parametric nature of the CRYOTE 2 experiments. Cases were chosen to assess the model's performance with respect to different variables such as initial fill levels, RT pressures, and wall superheats. The selected cases are

denoted in Table VIII with an asterisk in the 'Test' column. The first test, 20150227, was chosen to assess the model's performance with respect to higher initial vapor temperature. It was also the longest duration test that was modeled. 20160914, on the other hand, started at a much cooler state and with the lowest initial fill level but the highest initial RT pressure. The next case, 20161004, represents a more 'middle of the road' case with respect to the initial temperatures and pressures. It is also a relatively short test, similar to 20160914. The final two cases presented in the following section, 20161007 and 20161012, have the highest initial fill levels, each starting at more than 3% full. Each of the two tests are started in relatively chilled down tanks but the first of the two, 20161007, runs for a significantly longer time than 20161012 (700s vs 111s). As will be shown in the following figures, the reason for this discrepancy in fill times is likely the fact that the pressure does not stabilize at a low enough value for 20161012.

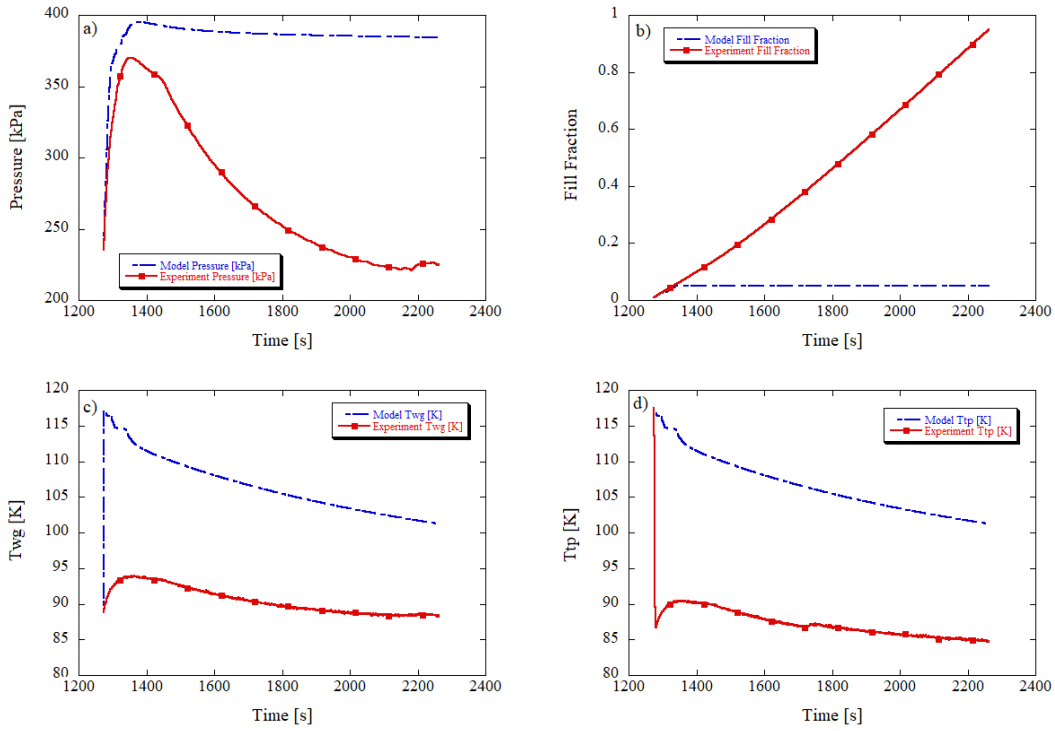

Figure 24: Model vs experiment results for the 20150227 CRYOTE 2 test. Subplot (a) shows pressure, (b) fill fraction, (c) wall-gas temperature, and (d) two-phase temperature.

The first case presented in Figure 24 represents a scenario with a relatively high initial vapor temperature as compared with the other tests presented here. This higher vapor temperature could be a contributing factor in the relatively less accurate pressure trace. While the initial pressure spike tracks the experiment, the model pressure does not recover in the same way. Likely, this is caused by an underestimation of the condensation at the interface as well as an elevated T_{wg}, as evidenced by Figure 24c. Because the tank pressure remained elevated, it is also likely that the mass flow rate into the tank stalled or what entered the tank flashed to, and remained, vapor. This would account for the poor fill fraction modeling performance shown in 24b. T_{tp} also remained comparatively high. This is somewhat anomalous compared to the other tests presented for CRYOTE 2 in this work and is likely caused by the poor

pressure prediction. Another possible explanation for the poor predictive performance is that, compared to the other cases that are presented, 20150227 also had a higher average mass flow rate, in addition to initial vapor temperature. It's possible that the condensation and wall chilldown rates were not sufficient to accurately 'keep up' with the mass inflow, thereby keeping the pressure elevated for the duration of the model.

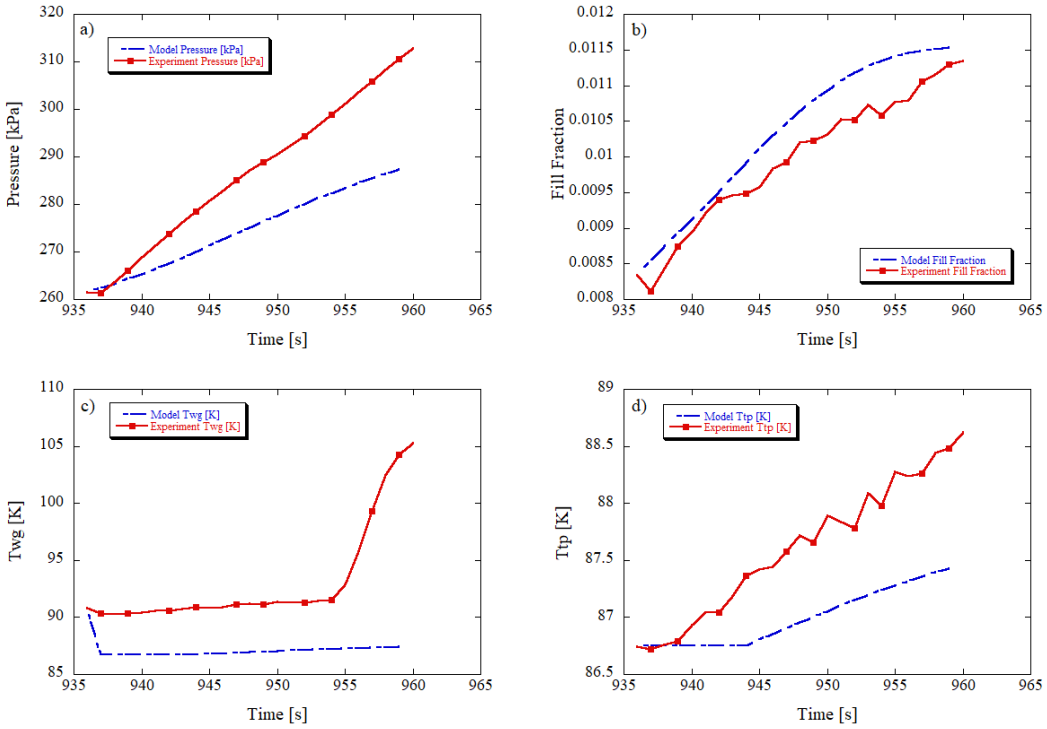

Figure 25: Model vs experiment results for the 20160914 CRYOTE 2 test. Subplot (a) shows pressure, (b) fill fraction, (c) wall-gas temperature, and (d) two-phase temperature.

Compared with test 20150227, 20160914 started in a relatively more cooled-down state with respect to vapor temperature in the receiver tank though the actual RT pressure was elevated. The cooled down nature of the tank is likely a large contributing factor in the strong model performance in this case, as evidenced by the fact that none of the reported MAPE's exceeded 7%. As shown in Figures 25a

- 25d, the model did under-predict the pressure response, though not dramatically given that the pressure error for this test was only 3.9%. This is likely due to the fact that the wall-gas and two-phase temperatures predicted by the model were below the experiment. While the two-phase temperature prediction is only slightly below the experiment, wall-gas temperature deviates more noticeably from the experimental values. Given that, it's not surprising to see that the pressure remains suppressed. This also likely explains the slightly higher fill fraction. Since more of the cryogen entering the tank is condensed, it will register as a having a greater liquid volume than if a larger fraction were to remain vapor. A possible explanation is the relatively low mass flow rate. If the condensation and chilldown rates were too high, flashing and boiling of the incoming cryogen might be under-predicted. Unfortunately, this does not fully explain the inaccuracy present in this case since, as will be shown in Figure 28, case 20161012 has a much more accurate pressure response despite having similar dynamics present between the fill fraction, T_{wg}, and T_{tp} variables. 20161012 also has the same average mass flow rate for the duration of the fill. Since the inflow data is fed in as a time-series, however, it is likely that there are differences at key parts of the filling process.

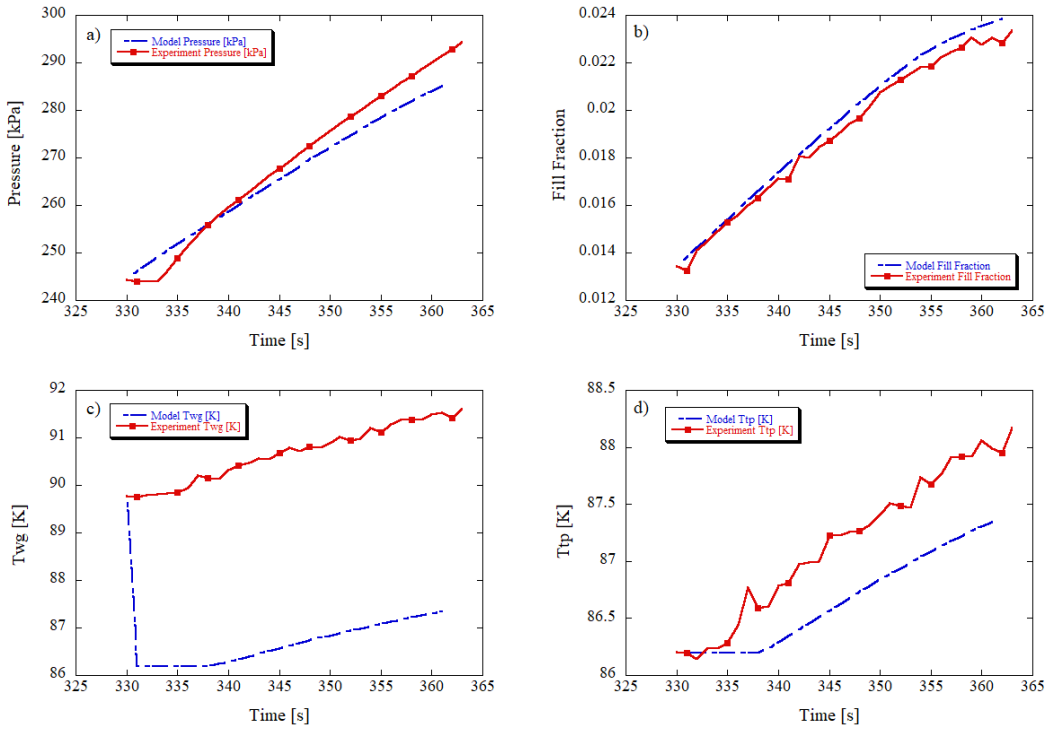

Figure 26: Model vs experiment results for the 20161004 CRYOTE 2 test. Subplot (a) shows pressure, (b) fill fraction, (c) wall-gas temperature, and (d) two-phase temperature.

For the 20161004 experiment, like the previous 20160914, the pressure trace presented during fill is not the characteristic trace that is often seen with an initial pressure spike, rollover, and then piston-cylinder spike. This is likely because the tank is starting in a chilled down state to begin so there is less flashing and boiling to cause the initial pressure spike. While there were some deviations present in fill fraction, T_{wg}, and T_{tp}, the model pressure response mirrored the experiment fairly well, including the absence of the initial pressure spike. As for the other variables, the deviations present between the model and experiment are not very large and did not appear to be a cause for concern. Overall, the model did well with the 20161004 case, given that error rates did not exceed 4.5%.

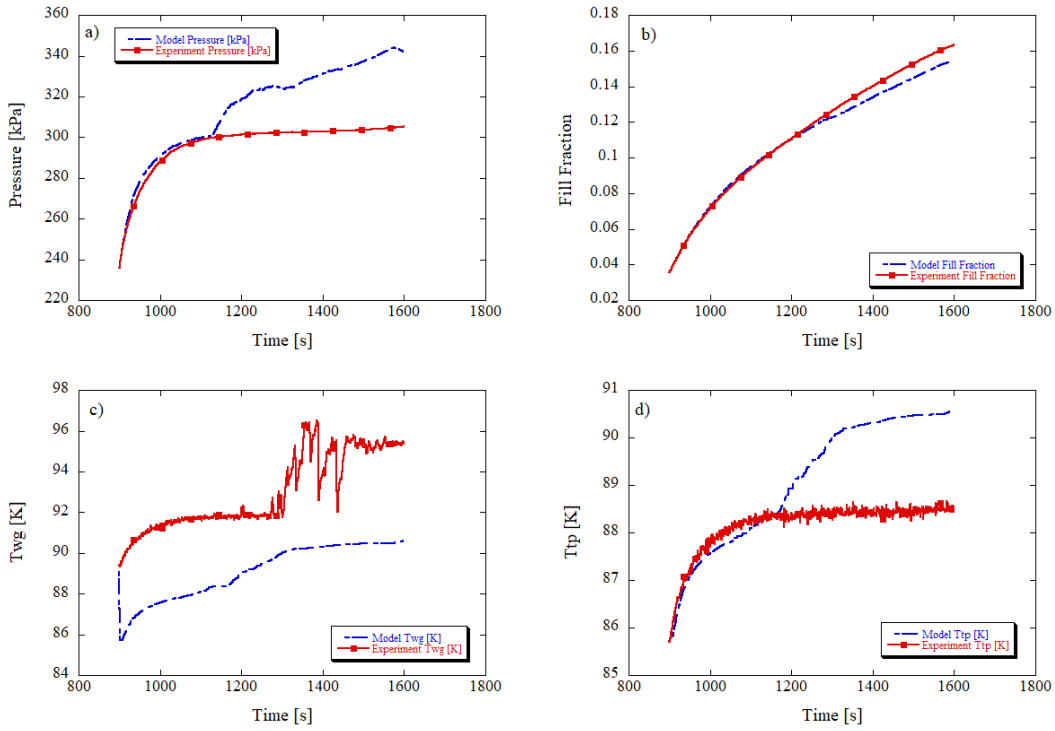

Figure 27: Model vs experiment results for the 20161007 CRYOTE 2 test. Subplot (a) shows pressure, (b) fill fraction, (c) wall-gas temperature, and (d) two-phase temperature.

Test 20161007 presented in Figure 27 was, relative to 20160914 and 20161004, a longer test. This allowed for more propagation of model errors. Interestingly, the model does relatively well with respect to pressure prediction until approximately 1150 seconds. It is at this point that there is an upward deviation from the experiment. This deviation is also present in T_{tp} as shown in Figure 27d. A possible explanation for this departure from the experiment is inaccuracy in the two-phase correlation. Because the two-phase temperature actually rises at the beginning of the test, it is possible that the error lies in the correlation used to model this transition from nucleate boiling to transition boiling, for example. Given the relative flatness of the experimental two-phase temperature, it seems plausible that a boiling regime transition did not occur. So if the model chose to start using transition or even

film boiling heat transfer approximations before what occurred in the experiment, it would cause a deviation. Unfortunately, without better spray cooling correlations for cryogenic liquids, it is difficult to improve these regime cutoff temperatures and the associated heat transfer correlations within a given regime. T_{wg} also appears to have deviated from the experimental value though it starts to 'recover' after its initial drop. It is important, however, to view these discrepancies in context. While the model did exhibit somewhat different behavior from the experiment, the error rates for 20161007 were all still at or below 6%, which indicates strong performance for two-phase modeling.

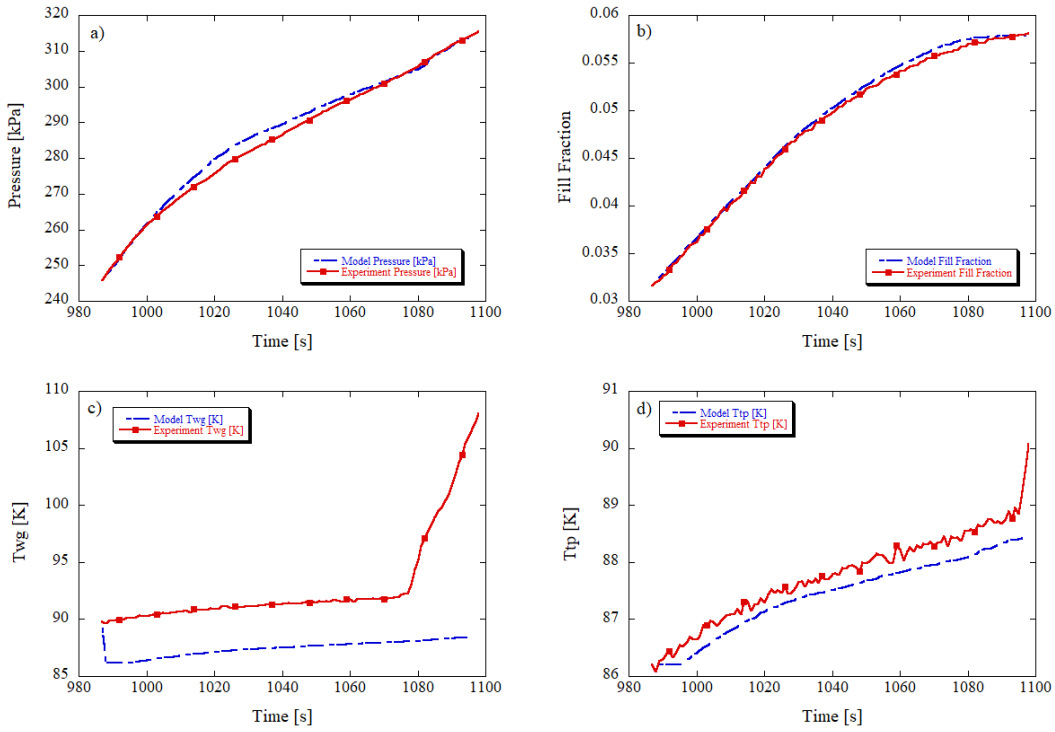

Figure 28: Model vs experiment results for the 20161012 CRYOTE 2 test. Subplot (a) shows pressure, (b) fill fraction, (c) wall-gas temperature, and (d) two-phase temperature.

The final CRYOTE 2 case presented in this work is 20161012. In this case, the model performed well with respect to all of the variables, though some deviation

is more obviously present in T_{wg}. This slight deviation might partly explain the differences in pressure traces though the error in pressure is small enough that there might be a number of minor contributing factors. One interesting detail that the model missed was the sharp temperature increases towards the end of the experiment. Given that the tank was not close to full as evidenced by Figure 28b, it is unclear what caused that temperature increase to occur in the experiment so its absence is harder to explain with respect to the model prediction. In a similar sense to case 20161007 though, the model did quite well with 20161012, exhibiting an error rate of no greater than 6% across all of the variables under inspection.

Table IX: Error rates for individual CRYOTE 2 tests.

Test	**Pressure MAPE**	**Fill MAPE**	T_{wg} **MAPE**	T_{tp} **MAPE**
20150218	0.414	0.705	0.146	0.191
20150227	0.447	0.773	0.178	0.222
20150303	0.210	0.996	0.014	0.057
20150304.2	0.502	0.962	0.516	0.572
20150309.2	0.480	0.966	0.591	0.652
20160914	0.039	0.039	0.062	0.007
20160921	0.186	0.640	0.009	0.037
20161004	0.012	0.020	0.043	0.005
20161006.1	0.208	0.557	0.011	0.031
20161006.2	0.209	0.558	0.011	0.033
20161006.3	0.008	0.005	0.052	0.004
20161007	0.060	0.026	0.042	0.012
20161012	0.005	0.007	0.057	0.004
Mean	**0.214**	**0.486**	**0.124**	**0.133**

Table IX shows the errors rates for all of the CRYOTE 2 cases considered in the correlation assessment. In comparing the results from Table IX with the model input

conditions in Table VIII, one thing that becomes clear is that the model performed significantly better on cases where the vapor and wall nodes were cooled down closer to saturation prior to initiating fill. The tests with the highest error, 20150218, 20150227, 20150304.2, and 20150309.2, all started with noticeably warmer vapor temperatures and wall temperatures. This may be indicative of a model shortcoming with respect to its ability to predict the chilldown and related boil-off at the wall at temperatures farther from saturation. That said, the model performs quite well on the chilled down cases, exhibiting a mean pressure rate of only 10.4%. The other variables, including initial fill level, initial RT pressure, and fill pressure appear to have a lower impact on the performance of the model prediction. When considering all CRYOTE 2 cases, the model had a 21.4% error rate with respect to pressure. Model temperature prediction did noticeably better with an average 13% error rate between T_{wg} and T_{tp}. Fill prediction performance, however, did significantly worse with an error rate of more than 48%. As noted in section 2.3, the non-equilibrium assumption for evaporation / condensation at the liquid-vapor interface improved the fill performance significantly. Future work could look at optimizing correlations specifically for CRYOTE 2-like cases if fill fraction prediction is an important parameter.

CHAPTER IV

Marshall Space Flight Center ASUS Experiments

4.1 Experimental Description

The primary objective of the Advanced Shuttle Upper Stage (ASUS) tests was to demonstrate a rapid chill and fill for a LH2 tank in an ambient environment [52]. Success criteria were defined as a vented chill and NVTO within 5 minutes. Tests were conducted in 2000 at the multipurpose hydrogen test bed (MHTB) at NASA MSFC. The RT used in these experiments was a 638.5 ft3 (18 m3) cylindrical aluminum tank with 2:1 elliptical dome ends. The tank was 10 ft (3.3 m) in height with a diameter of the same dimension and a wall thickness of 0.5 in (1.25 cm). As illustrated in Figure 29, thermal protection consisted of both spray-on foam insulation and variable density multilayer insulation.

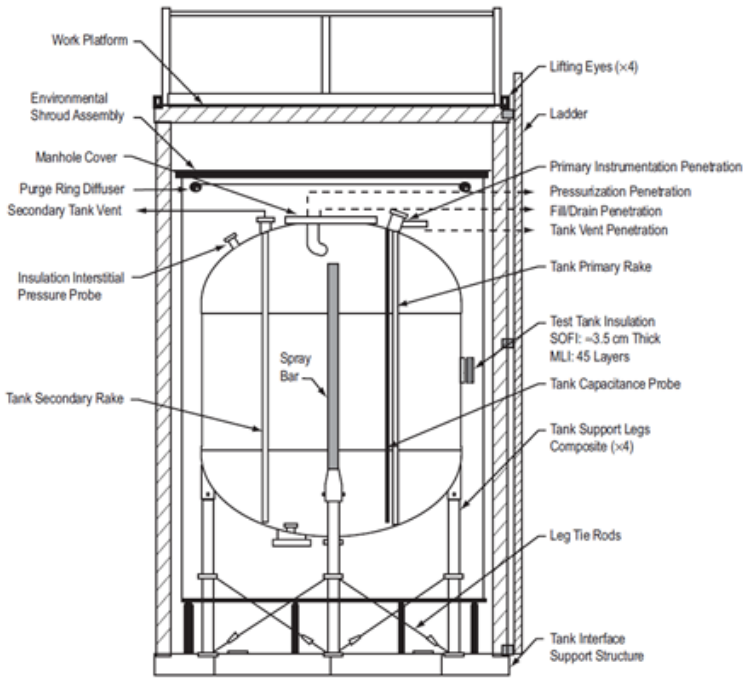

Figure 29: Multi-purpose hydrogen test bed setup for the Advanced Shuttle Upper Stage Experiments. Originally published in [52]

The tank was supported on composite legs designed to minimize heat leak. Additionally, the RT was surrounded by a shroud to minimize condensation on the tank and decrease the thermal gradient between the tank and its surroundings. Prior to conducting any tests, the tank itself was conditioned using dry nitrogen. Gaseous hydrogen was then used to purge any remaining nitrogen in the tank. This process was repeated until the tank temperature reached 294 +/- 5.6 K.

The cryogen transfer line and spray bar were capable of delivering up to 4.16 m3/min of LH2 into the tank. To prevent over-pressurization during the NVTO, a threshold pressure of 324 kPa was established; if the ullage pressure rose above this setpoint, the test would be terminated. The test would also be finished if the fill level exceeded 90% as determined by the capacitance probe located in the receiver tank.

In total, 14 tests were conducted. The first eight tests were checkout tests while the remaining six were performance tests. The checkout tests were conducted to verify

the performance of the test hardware and to characterize the system operation with LH2. The performance tests were then conducted to establish chilldown performance. Of these 14 tests, however, only five included NVTO attempts. The UNVF model, therefore was used to simulate only these five cases, though the final two cases (Test 13 and Test 14) were split into two separate fill sections as shown in Table XI. The experimental test matrix originally presented in Flachbart et al [52] is reproduced here for reference in Table X.

Table X: Experimental test matrix for Advanced Shuttle Upper Stage checkout and performance testing

	Test Number	**Description**	**Supply Pressure**		**MHTB Peak Pressure**		**Fill Level**
	#	–	*psia*	*kPa*	*psia*	*kPa*	%
Checkout Tests	1	LN_2 cold shock	0.3	99	N/A	N/A	N/A
	2	Vented fill	12	184	9.9	170	6
	3	Vented fill	11.9	183	9.8	167	31
	4	Vented fill	32.8	327	24.3	269	63
	5	Vented fill	32.8	327	24.4	270	99
	6	Vented fill	42.9	397	28.6	299	98
	7	Vented fill/ attempted no-vent fill	42.9	397	28.2	296	98
	8	Vented fill	36.8	355	27.7	292	13
Performance Tests	9	Vented fill	44.9	411	26.6	285	91
	10	Vented fill/ attempted no-vent fill	44.9	411	27.2	289	90
	11	Vented fill	44.8	410	27.4	290	90
	12	Vented fill/ attempted no-vent fill	44.8	410	26.3	283	(a) 90, (b) –, (c) –
	13	Vented fill/ attempted no-vent fill	44.8	410	26.8	286	(a) 90, (b) 73, (c) 83
	14	Vented fill/ attempted no-vent fill	44.8	410	26.2	282	(a) 90, (b) 79, (c) 90

As noted in Table X, five experiments were conducted which included NVTO. In each of these tests, the RT started with some initial amount of liquid in the tank. In Table X, the MHTB Peak Pressure refers to the initial pressure as the empty tank fill began and for Tests 12-14, (a) denotes the vented fill level, (b) is the level to which is tank is drained, and (c) is the level achieved after the refill attempt with the vent

closed. To initialize the model correctly, it is necessary to input starting conditions as accurately as possible. These conditions for tests 7, 10, 12, 13, and 14 are listed in Table XI.

Table XI: Advanced Shuttle Upper Stage model initial conditions

Test	T_{supply}	P_{supply}	**Initial Tank Pressure**	**Test Duration**	**Tank Wall Temp**	**Tank Vapor Temp**	**Initial Fill Level**	**Initial Liquid Temp**	$\dot{m}$
#	K	kPa	kPa	s	K	K	%	K	kg/s
7	21.18	250.02	141.19	8.1	67.68	21.77	90.06	21.49	5.02
10	21.38	263.51	147.45	14	87.95	31.21	82.25	21.53	4.97
12	23.38	248.90	135.74	30.1	65.90	26.13	87.31	21.34	0.098
13a	23.41	246.14	136.60	2.8	65.92	26.72	86.91	21.34	5.89
13b	22.63	271.83	118.84	137.1	23.28	34.55	68.94	20.66	1.70
14a	23.35	250.99	128.89	2.7	23.19	26.68	85.75	21.17	14.82
14b	22.08	302.46	119.32	112.8	21.57	33.20	79.09	20.70	1.76

4.2 Model Inputs / Considerations

The following section provides a mapping from the raw data fields provided from the ASUS experiments to those used for the UNVF model. To start, the receiver tank pressure with respect to time was recorded on sensor 100531P42. The liquid level in the tank with respect to time was provided by 1027LL1. In order to get the liquid mass at any time, it was necessary to calculate the liquid density. This was calculated differently depending on whether enough liquid had accumulated to reach the bottom-most thermocouple (TD24). When liquid has not yet reached TD24 thermocouple, the liquid density was calculated with REFPROP using the average of inlet temperature (100231T37, which assumes single phase liquid) and saturation temperature along with ullage pressure (100531P42). In the case where liquid had reached TD24 (determined by TD24 reading being lower than saturation temperature at tank pressure), liquid density calculation uses TD24 reading and the ullage pressure. The vapor or ullage density was calculated by REFPROP using ullage pres-

sure and the estimated ullage temperature. To estimate the ullage temperature, an average of T_{sat} at ullage pressure (a REFPROP quantity) and the temperature at the highest TC (TVL4). The liquid and gas masses could then be calculated according to equations 4.1 and 4.2.

$$m_l = \rho_l V_{RT} LL_i \tag{4.1}$$

$$m_v = \rho_{ullage} V_{RT} \left(1 - LL_i\right) \tag{4.2}$$

To get the inlet mass flow rate, the inlet volumetric flow rate (1046FM3125) was multiplied by the inlet density. Flow density is calculated using REFPROP at flow meter downstream pressure (104831P35) and flow meter downstream temperature (100731T33).

Temperature sensors 1109TW1 – 1109TW6 define the tank wall temperatures. For the sake of model comparison, TW4, which is at 56.5% fill, is compared with T_{tp} while TW5 (76.7%) fill is compared with T_{wg}. An initial mass averaged wall temperature which considers both the tank wall (1109TW1-1109TW6) and the lid (1075TMN1) is calculated according to equation 4.3.

$$T_{RT,avg} = \frac{\sum_{i=1}^{n} T_i \Delta m_i}{m_{RT}} \tag{4.3}$$

The inlet state of the fluid is simply defined using the inlet pressure (100131P39) and the inlet temperature (100231T37). Finally, the initial conditions within the tank are defined by the silicon diode at 4.3% fill (1090TD13) for the liquid temperature and by 1090TD24 for the ullage temperature.

4.3 Results

For the sake of brevity and concision, it was decided not to plot two of the seven ASUS cases. Specifically, Tests 13a and 14a were excluded. Given the very brief

duration of these tests, it was concluded that this would not serve as a significant detriment to the usefulness of this analysis.

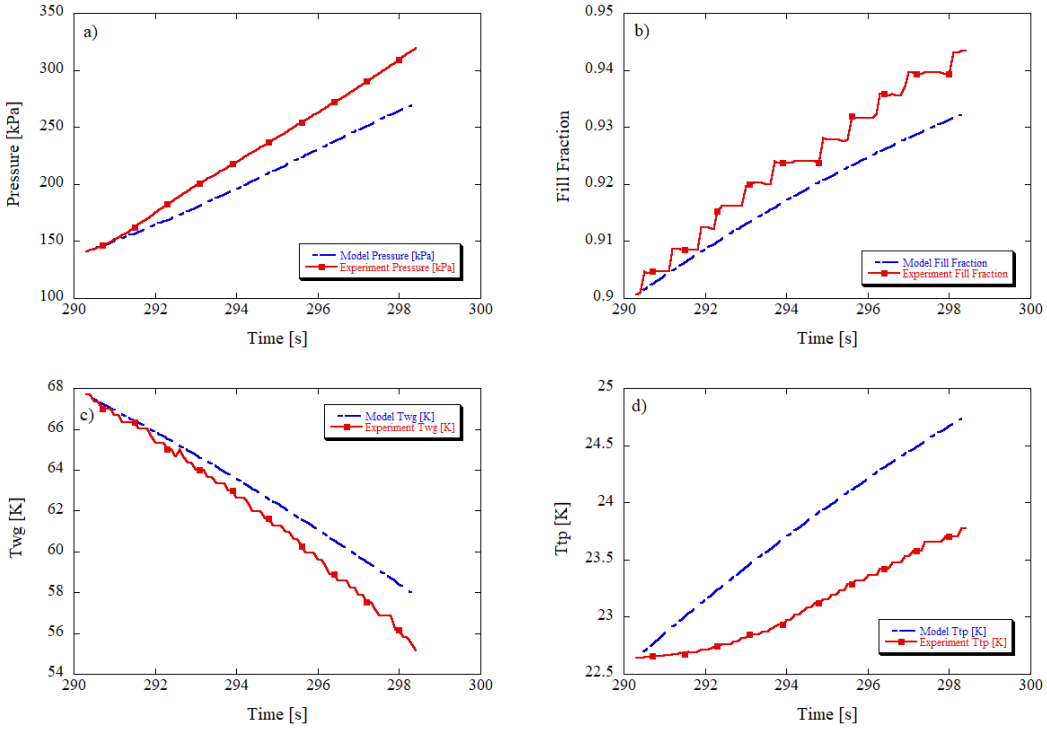

Figure 30: Model vs experiment results for test 7 from the Advanced Shuttle Upper Stage experiments. Subplot (a) shows pressure, (b) fill fraction, (c) wall-gas temperature, and (d) two-phase temperature.

The first test plotted from the ASUS experiments is test 7 as shown in Figures 30a - 30d. Relative to the experiment, the model under-predicts the pressure within the receiver tank, though the nominal error rates are still reasonably good at less than 10%. The under-prediction of the pressure is somewhat unexpected when taken in conjunction with Figures 30c and 30d which both show the model predicted temperatures higher than the experiment. In the situation where the model temperatures are higher, one would expect a higher pressure as well since higher temperatures are more likely to lead to more evaporation and boil-off and less condensation. One possible explanation for this is that the mass inflow data was slightly incorrect. If the mass

inflow to the model were below the actual experimental inflow, it's possible that the thermodynamic response would be altered enough to produce the plots in Figure 30. This is somewhat corroborated by Figure 30b, which shows the model fill fraction below the experiment though not significantly.

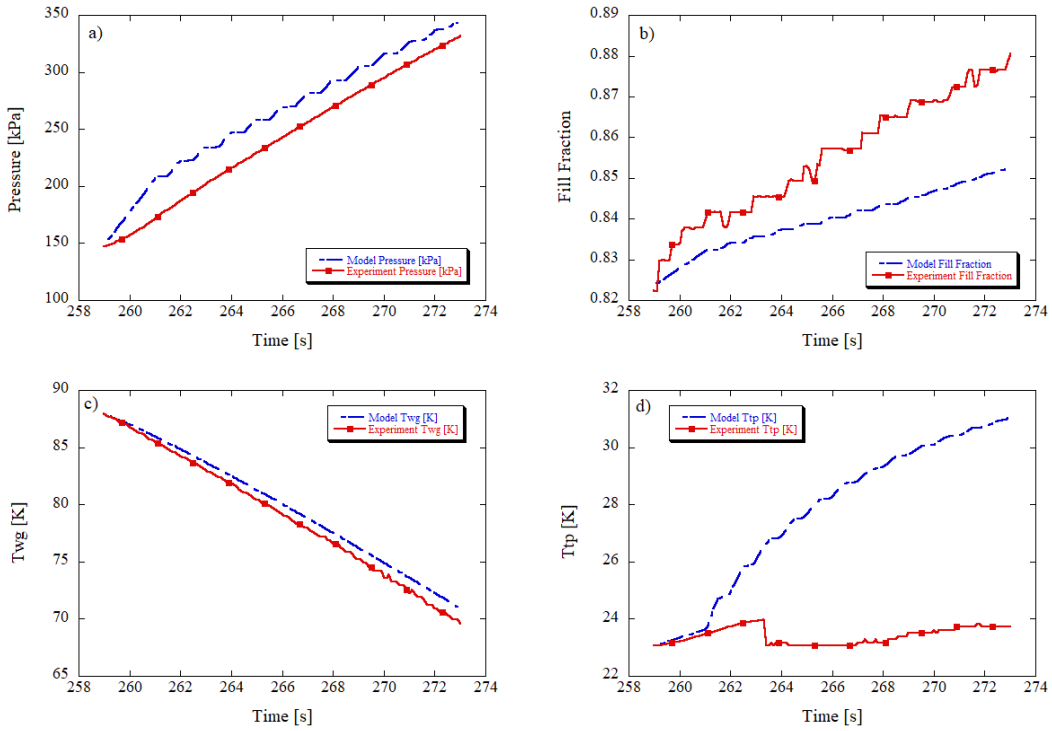

Figure 31: Model vs experiment results for test 10 from the Advanced Shuttle Upper Stage experiments. Subplot (a) shows pressure, (b) fill fraction, (c) wall-gas temperature, and (d) two-phase temperature.

For test 10, there is reasonable agreement between the model and the experiment with respect to the pressure and T_{wg} traces. While the model slightly over-predicts pressure, it remains relatively consistent after approximately 261 seconds and only exhibits an error rate of 9.2%. At around the same time, T_{tp} deviates from the experiment noticeably. Instead of tracking between 23 and 24 K, the model two-phase temperature shows a clear and steady increase. It is possible that the temperature that marked the divergence from the experiment also represented a change in the

boiling regime. If h_{tp} decreased with the change in regime, it is possible it caused this increase in T_{tp}. Discrepancy also exists in the fill fraction as shown in Figure 31b. Ultimately, there appears to be about a 2% difference in the final fill levels. This may be due to increased boil-off caused by the higher two-phase temperature.

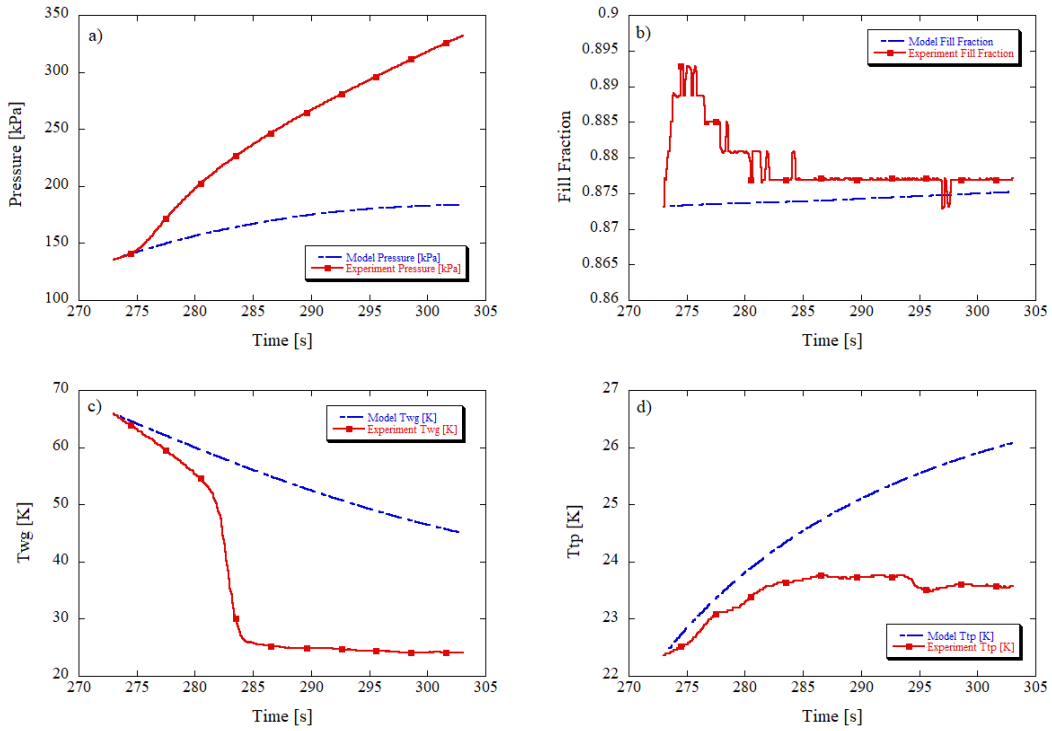

Figure 32: Model vs experiment results for test 12 from the Advanced Shuttle Upper Stage experiments. Subplot (a) shows pressure, (b) fill fraction, (c) wall-gas temperature, and (d) two-phase temperature.

Compared to tests 7 and 10, test 12 performed noticeably worse in most categories. Model pressure significantly under-predicts experimental while both T_{wg} and T_{tp} are higher than experimental. As can be seen in Table XI, the initial condition for test 12 are not significantly different than those of tests 7 and 10 so it is unlikely that the temperature deviation from experiment is caused by dramatic differences in initial tank state. A contributing factor is likely sensor selection. The experimental plots for both T_{wg} and T_{tp} bottom out, indicating that the sensor may have become

submerged. Another possible explanation for the discrepancy in temperature performance comes from the fill fraction plot. The clear deviation from the experiment and the noise that seems to be present in the experimental data suggest that there may have been extraneous experimental influences during the test. The model mass inflow was estimated based on the average inflow during the test period but the increasing and subsequent decreasing of the fill fraction within the receiver tank suggests either sensor error or other experimental nonconformances. Given the noise present in this case, it is unreasonable to assume the model would have been able to accurately predict such deviations from the norm.

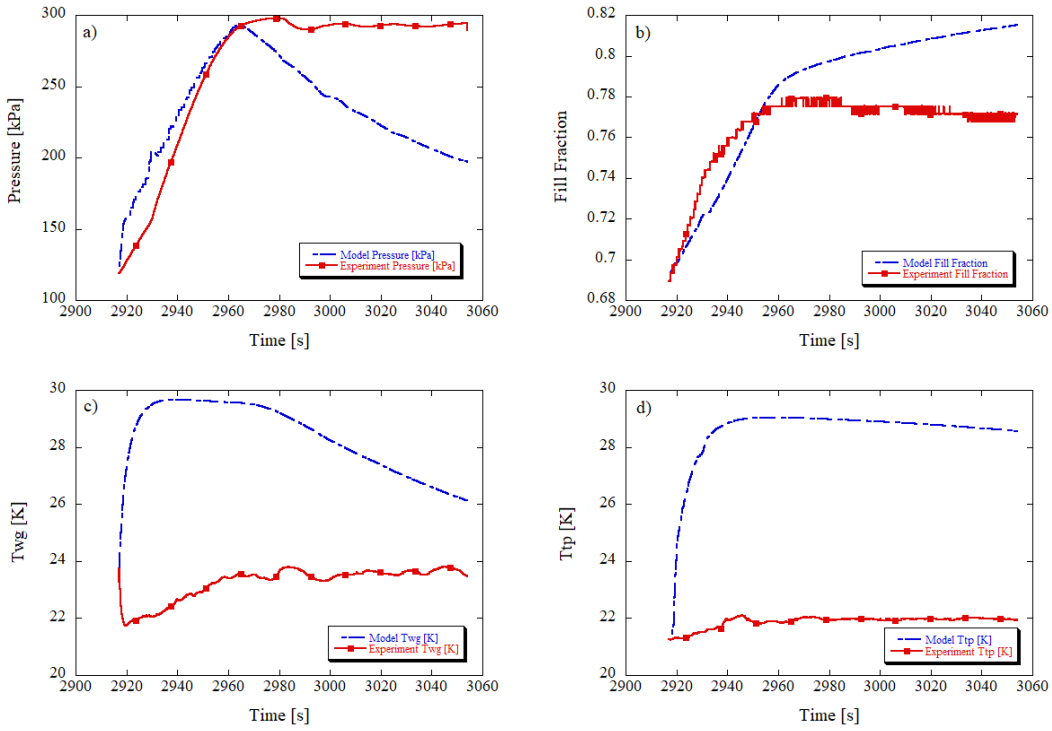

Figure 33: Model vs experiment results for test 13b from the Advanced Shuttle Upper Stage experiments. Subplot (a) shows pressure, (b) fill fraction, (c) wall-gas temperature, and (d) two-phase temperature.

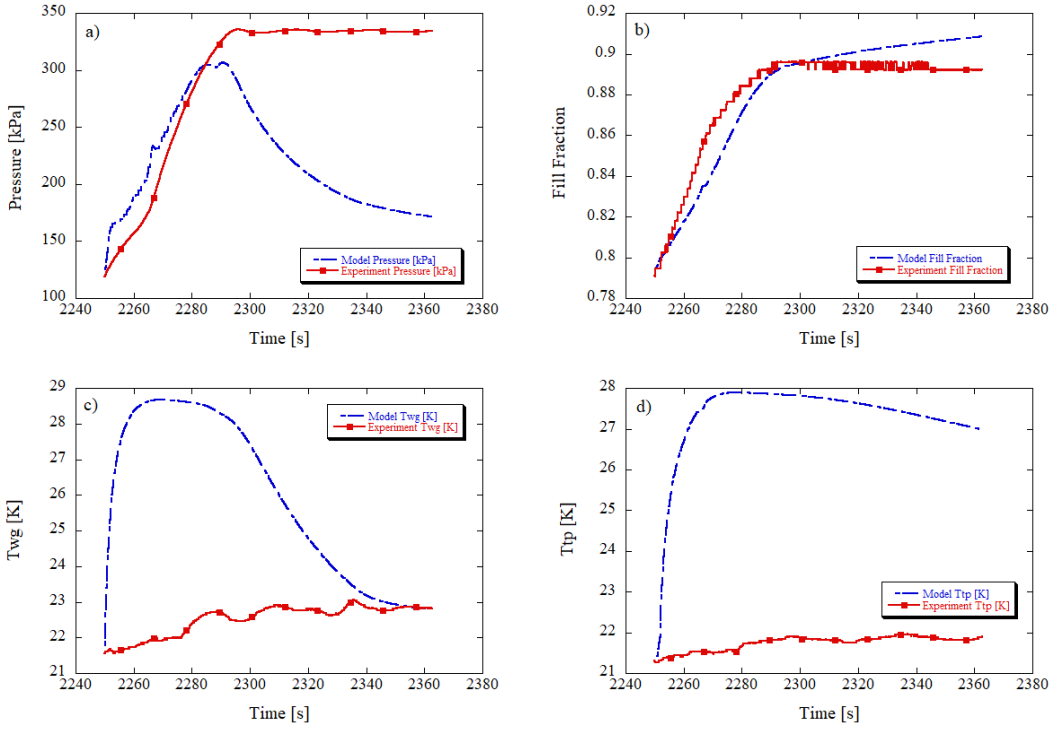

Figure 34: Model vs experiment results for test 14b from the Advanced Shuttle Upper Stage experiments. Subplot (a) shows pressure, (b) fill fraction, (c) wall-gas temperature, and (d) two-phase temperature.

Tests 13b and 14b both exhibit very similar responses during the NVTO. Each does a reasonable job predicting the initial pressure spike within the tank as shown in Figures 33a and 34a. In addition to accurately predicting the slope of the increase, the model is close to the experiment with respect to the magnitude of the maximum pressure. Following this max pressure event, however, the model and the experiment deviate from each other. For both tests, the model exhibits somewhat 'typical' NVF/NVTO behavior in that the pressure spike is followed by a collapse, indicative of condensation occurring within the tank. In the experiments, however, the pressure remains elevated for the remaining duration of the test. Given the similarity in fill fraction estimates from the model versus the experiment, this is an interesting result. One would expect that the fill would slow in the case of the experiment if the the

tank pressure became closer to the inlet pressure based on Equation 1.7. This does not appear to be the case however in the experiments suggesting that condensation in the tank must have been adequate to manage any vapor introduced through flashing or boil-off. The model also behaved similarly in both cases with respect to the two-phase and wall-gas temperatures. In both instances, T_{wg} and T_{tp} are noticeably above the experimental values. As noted previously, this is possibly due to the inherent challenges in comparing a node with homogeneous temperature distribution to a static sensor. Regardless, the elevated model temperatures do not appear to have impacted the pressure trace in the expected manner which would be to cause a pressure increase. At least, any associated pressure increase due to the elevated temperatures did not compensate enough for the model pressure to converge with the experiment in the latter half of the tests. Compared with the previous tests, tests 13b and 14b are significantly longer in duration. It's possible that the divergence that is shown after the initial pressure spike might have become evident if the original tests were conducted for longer periods of time / started at lower initial fill values.

The final error rates for all of the ASUS tests are reported below in Table XII. While the model clearly performed better for some cases as compared to others, the overall error rates for all cases were promising. In comparing the error rates from Table XII to the initial conditions in Table XI, there does not appear to be a distinguishing variable that might indicate performance. For example, the model appeared to do well in cases with both high and low tank wall temperatures. The only variable that seems to correlate loosely with model performance is initial tank pressure. In cases with slightly higher initial tank pressures, the model performed better. For all cases, the mean pressure error rates of 15.9% is well within the typically accepted error rates of 25% or so for two-phase predictive models. Similarly, fill fraction error rates were, on average, very low for all cases. Overall, the model did well predicting the ASUS

tank response in cases with high initial fill levels though some divergence did occur for longer duration tests that started below 80% initial fill level.

Table XII: Error rates for individual Advanced Shuttle Upper Stage tests.

Test	**Pressure MAPE**	**Fill MAPE**	T_{wg} **MAPE**	T_{tp} **MAPE**
Test 7	0.098	0.007	0.024	0.034
Test 10	0.092	0.019	0.010	0.199
Test 12	0.289	0.006	0.716	0.052
Test 13a	0.114	0.113	0.109	0.140
Test 13b	0.163	0.031	0.220	0.304
Test 14a	0.082	0.091	0.096	0.103
Test 14b	0.277	0.014	0.157	0.257
Mean	**0.159**	**0.040**	**0.190**	**0.156**

CHAPTER V

Conclusion

On-orbit refueling of cryogenic propellants is a key technological enabler for long-duration space missions. Current methods of cryogenic refueling are suboptimal for fuel-efficient transfers because of their need to vent. The unknown location of the liquid and vapor phases in the receiver tank means it is possible to vent liquid – an extremely wasteful proposition for any payload launched from Earth. One option is to 'settle' the tanks whereby the spacecraft accelerates to force the liquid phase to a known location. The downside of this approach is it requires propellant or power to induce the necessary thrust for the acceleration. A more desirable alternative is to use the propellant itself to manage the pressure response in the receiver tank by condensing the vapor produced by boil-off and evaporation. This approach is known as no-vent fill (NVF) or no-vent top-off (NVTO) .

This work sought to improve upon an existing model for NVF/NVTO by conducting a thorough trade study related to the underlying correlations used for heat transfer at various points in the NVF/NVTO. The correlations that were tested predict the heat transfer due to natural convection between the ullage and tank wall as well as at the interface. Two-phase cooling was also investigated where the propellant droplets impinge upon the tank well. Finally, heat transfer between the droplets themselves and the ullage and the evaporation / condensation at the liquid-vapor

interface was examined. To evaluate the effectiveness of a given set of correlations, the model was used to predict the pressure and temperature response for 34 different experimental tests. This work examined two distinct experiments, presenting 21 of the 34 tests.

The final correlation set that was chosen had a mean error rate of approximately 25.9% across all 34 tests for pressure response. On the tests specifically under inspection in this work, the mean average percentage error for pressure response prediction was 21.4% and 15.9% for the CRYOTE 2 and ASUS tests, respectively. For temperature response prediction, the overall error rate was 29.5% for wall-gas temperature and 24.9% for two-phase temperature. These represent a 31% improvement over the worst correlation set that was tested with respect to pressure. This model may be further improved by conducting a broader assessment which tests both droplet heat transfer correlations and tests the equilibrium assumption for each correlation set. While computationally intractable for this work, a broader assessment may improve the fill prediction performance while maintaining the pressure prediction performance. Additionally, the model's usefulness could be further improved by evaluating it against experiments conducted with propellants other than LN2 or LH2.

Given the rapidly accelerating pace of change in space travel and the increased expectations associated with long term space travel, the improved model presented in this work will be able to aid development with more accurate pressure predictions and temperature response within receiver tanks in 1-g scenarios. This improved prediction ability may help reduce design and testing times and enable the quicker iterations needed to advance on-orbit refueling capability.

BIBLIOGRAPHY

[1] Mul, J., Korting, P., and Schoeyer, H. (1990). Search for new storable high-performance propellants. ESA journal, 14(3), 253-270.

[2] Barron, R. F. (1966). *Cryogenic systems*. New York: McGraw-Hill.

[3] Panzarella, C., and Kassemi, M. (2005). Self-Pressurization of Large Spherical Cryogenic Tanks in Space. Journal of Spacecraft and Rockets, 42(2), 299-308.

[4] Chato, D. (2005). Low Gravity Issues of Deep Space Refueling. 43rd Aerospace Sciences Meeting and Exhibit. American Institute of Aeronautics and Astronautics Inc, AIAA.

[5] Ross, R. and Boyle, Robert. (2002). NASA Space Cryocooler Programs—An Overview. 10.1007/0-306-47919-2 1.

[6] Hartwig, J.W. (2015). *Liquid Acquisition Devices for Advanced In-Space Cryogenic Propulsion Systems*. Elsevier: Boston, MA.

[7] Hartwig, J.W. (2022). Development and Validation of a Numerical Thermodynamic Non-Equilibrium Model for Cryogenic No-Vent Fill Operation.

[8] Aerospace Corporation (1971). Orbiting Propellant Depot Safety, Vols.1-3. Aerospace Report No. ATR-71 (7223)-3.

[9] Howell, J., Mankins, J., and Fikes, J. (2006). In-Space Cryogenic Propellant Depot Stepping Stone. Acta Astronautica, 59(1-5), 230-235.

[10] Schweickart, R. (2014). Thermodynamic analysis of a demonstration concept for the long-duration storage and transfer of cryogenic propellants. Cryogenics, 64, 283-288.

[11] (2019). *SINDA/FLUINT General Purpose Thermal/Fluid Network Analyzer.*

[12] Chato, D.J. (1991). Ground Testing on the Nonvented Fill Method of Orbital Propellant Transfer: Results of Initial Test Series. NASA-TM-104444.

[13] Chato, D.J., Moran, M.E., and Nyland, T.W. (1990). Initial Experimentation on the Nonvented Fill of a 0.14 m3 Dewar with Nitrogen and Hydrogen. NASA-TM-102155.

[14] Chato, D.J. (1993). Ground Testing for the No-Vent Fill of Cryogenic Tanks: Results of Tests for a 71 Cubic Foot Tank. NASA-TM-106293.

[15] Moran, M.E., Nyland, T.W., and Driscoll, S.L. (1991). Hydrogen No-Vent Fill Testing in a 1.2 Cubic Foot (34 Liter) Tank. NASA-TM-105273.

[16] Moran, M.E., and Nyland, T.W. (1992). Hydrogen No-Vent Fill Testing in a 5 Cubic Foot (142 Liter) Tank Using Spray Nozzle and Spray Bar Liquid Injection. NASA-TM-105759.

[17] Yang, H., and West, J. (2015). CFD Extraction of Heat Transfer Coefficient in Cryogenic Propellant Tanks. 51st AIAA/SAE/ASEE Joint Propulsion Conference. American Institute of Aeronautics and Astronautics Inc, AIAA.

[18] Long, Z., and Zhang, P. (2014). Natural convection heat transfer of supercritical helium in a closed vertical cylinder. Cryogenics, 61, 120-126.

[19] Daney, D. (1975). Turbulent Natural Convection of Liquid Deuterium, Hydrogen, and Nitrogen within Enclosed Vessels. International Journal of Heat and Mass Transfer, 19(4), 431-441.

[20] McAdams, W.H. (1985). *Heat Transmission 3rd Edition*. Krieger Pub Co.

[21] Eckert, E.R.G., and Jackson, T.W. (1950). Analysis of Turbulent Free-

Convection Boundary Layer on Flat Plate. Technical Note 2207. National Advisory Committee for Aeronautics, NACA.

[22] Guyer, E., and Brownell, D. (1989). *Handbook of applied thermal design*. McGraw-Hill.

[23] Chow, M.Y., and Akins, R.G. (1975). Pseudosteady-State Natural Convection Inside Spheres. International Journal of Heat and Mass Transfer, 97(1), 54-59.

[24] Mattor, E.E., and Durgin, W.W., and Bloznalis, P. (1992). Analysis of Natural Convection in a Low Gravity Environment. 30th Aerospace Sciences Meeting & Exhibit. American Institute of Aeronautics and Astronautics Inc, AIAA.

[25] Memory, S.B., Adams, V.H., and Marto, P.J. (1997). Free and Forced Convection Laminar Film Condensation on Horizontal Elliptical Tubes International Journal of Heat and Mass Transfer 14, 3395 – 3406.

[26] Mudawar, I. (2001). Assessment of high-heat-flux thermal management schemes. IEEE Trans. Compon. Packag. Technol. 24, 122-141.

[27] Berenson, P.J. (1961). Film-Boiling Heat Transfer From a Horizontal Surface. Journal of Heat Transfer. 83(3). 351-356.

[28] Rini, D.P., Chen,R., and Chow, L.C. (2001). Bubble Behavior and Nucleate Boiling Heat Transfer in Saturated FC-72 Spray Cooling. ASME. J. Heat Transfer. 124(1). 63–72.

[29] Sehmbey, M.S., Chow, L.C., Hahn, O.J., and Pais, M.R. (1995). Effect of spray characteristics on spray cooling with liquid nitrogen. Journal of Thermophysics and Heat Transfer. 9(4). 757-765.

[30] Sehmbey, M.S., Chow, L.C., Hahn, O.J., and Pais, M.R. (1995). Spray cooling of power electronics at cryogenic temperatures. Journal of Thermophysics and Heat Transfer. 9(1). 123-128.

[31] Awonorin, S.O. (1989). Film boiling characteristics of liquid nitrogen sprays on a heated plate. International Journal of Heat and Mass Transfer. 32(10). 1853-1864.

[32] Liang, G. and Mudawar, I. (2017). Review of spray cooling – Part 1: Single-phase and nucleate boiling regimes, and critical heat flux. International Journal of Heat and Mass Transfer. 115. 1174-1205.

[33] Liang, G. and Mudawar, I. (2017). Review of spray cooling – Part 2: High temperature boiling regimes and quenching applications. International Journal of Heat and Mass Transfer. 115. 1206-1222.

[34] Lei, W., Zhang, F., and Yanzhoung, L. (2015). Performance Analysis of No-Vent Fill Process for Liquid Hydrogen Tank in Terrestrial and On-Orbit Environments. Cryogenics. 72. 161-171.

[35] Baumeister, K.J. and Simon, F.F. (1973). Leidenfrost Temperature: its correlation for liquid metals, cryogens, hydrocarbons, and water. Journal of Heat Transfer. 95(2). 166-173.

[36] Lienhard, J. and Dhir, V. (1973). Hydrodynamic Prediction of Peak Pool-Boiling Heat Fluxes from Finite Bodies. Journal of Heat Transfer. 95(2). 152-158.

[37] Shirai, Y., Tatsumoto, H., Shiotsu, M., Hata, K., Kobayashi H., and Naruo, Y. (2010). Boiling heat transfer from a horizontal flat plate in a pool of liquid hydrogen. Cryogenics. 50(6-7). 410–416.

[38] Minchenko, F.P., Bodrovich, B.I., and Borishansky, V.M. (1961). Heat transfer during nucleate boiling of water and ethyl alcohol, in a volume of collection of articles. S.S. Kutateladze (Ed.), Aspects of Heat Transfer and Hydraulics of Two-Phase Mixtures. Govt. Energy Publishing House, Moscow. 75–93.

[39] Wang, L., Wang, J., Yan, T., Ye, S., Xie, F., and Li Y. (2020). Heat Transfer prediction of liquid nitrogen film boiling from different heaters. International Journal of Multiphase Flow. 129.

[40] Majumdar, A., LeClair, A., Martin, A., Rhys, N., and Hartwig, J.W. (2020). Numerical Modeling of No Vent Fill of a Cryogenic Tank. AIAA-2020-3797, 2020 Joint Propulsion Conference New Orleans, LA.

[41] Mudawar, I. and Valentine, W.S. (1989). Determination of the Local Quench Curve for Spray-Cooled Metallic Surfaces. Journal of Heat Treating. 7. 107-121.

[42] Klingzing, W.P., Rozzi, J.C., and Mudawar, I. (1992). Film and Transition Boiling Correlations for Quenching of Hot Surfaces with Water Sprays. Journal of Heat Treating. 9. 91-103.

[43] Incropera, F. P., and DeWitt, D. P. (2002). Fundamentals of heat and mass transfer. New York: J. Wiley.

[44] Whitaker S. (1972). Forced convection heat transfer correlations for flow in pipes, past flat plates, single cylinders, single spheres, and flow in packed beds and tube bundles. AIChE Journal. 18. 361–371.

[45] Zhang, L., Li, Y.R., Zhou, L.Q., and Wu, CM. (2017). Comparison study on the calculation formula of evaporation mass flux through the plane vapour-liquid interface. Journal of Physics: Conf. Series 925. 012-019.

[46] Kartuzova, O. and Kassemi, M. (2011). Modeling Interfacial Turbulent Heat Transfer during Ventless Pressurization of a Large Scale Cryogenic Storage Tank in Microgravity. 47th AIAA/ASME/SAE/ASEE Joint Propulsion Conference Exhibit. American Institute of Aeronautics and Astronautics Inc, AIAA.

[47] Bellur, K. (2018). A New Technique to Determine Accommodation Coeffifficients of Cryogenic Propellants.

[48] Thomas, L.B. and Olmer, F. (1943). The Accommodation Coefficients of He, Ne, A, H2, D2, O2, CO2, and Hg on Platinum as a Function of Temperature. J. Am. Chem. Soc. 65 (6). 1036–1043.

[49] Bellur, K., Medici, E.F., Kulshreshtha, M., Konduru, V., Tyrewala, D., Tamilarasan, A., McQuillen, J., Leao, J.B., Hussey, D.S., Jacobson, D.L., Scherschligt, J., Hermanson, J.C., Choi, C.K., and Allen, J.S. (2016). A new experiment or investigating evaporation and condensation of cryogenic propellants. Cryogenics. 74. 131-137.

[50] Chato, D.J., and Sanabria, R. (1991). Review and Test of Chilldown Methods for Space-Based Cryogenic Tanks. NASA-TM-104458.

[51] Hartwig, J.W., Rhys, N., Clark, J., Mercado, M., LeClair, A., and Majumdar, A. (2021). Test Data Analysis of the Vented Chill, No-Vent Fill Liquid Nitrogen CRYOTE-2 Experiments. International Journal of Heat and Mass Transfer 167, 120781.

[52] Flachbart, R.H., Hedayat, K.A., Holt, J. Sims, Johnson, E.F., Hastings, L.J., and Lak, T. (2013). Large-Scale Liquid Hydrogen Tank Rapid Chill and Fill Testing for the Advanced Shuttle Upper Stage Concept. NASA/TP—2013–217482.

[53] Wood, J.J., and Foster, L.W. (2013). Acoustic and Thermal Testing of an Integrated Multilayer Insulation and Broad Area Cooling Shield System. Space Cryogenics Workshop.

[54] Rhys, N.O., Foster, L.W., Wood, J.J., Valenzuela, J.G., and Martin J.J. (2019). Vibro-Acoustic Test Article (VATA) Test Series. NASA-M19-7657.

[55] Marquardt, E.D., Le, J.P., and Radebaugh, R. (2000). Cryogenic Material Properties Database. 11th International Cryocooler Conference, Keystone, CO.

[56] Titanium Metals Corporation. Properties and Processing of TIMETAL 6-4.

[57] Hartwig, J.W., Johnson, W.L., Bamberger, H.H., Meyer, M.L., Wendell, J., Mullins, J., Robinson, R., and Arnett, L. (2020a). NASA Glenn Research Center Creek Road Cryogenic Complex: Testing between 2005 – 2019. Cryogenics. 106. 103038.